Observing Upper Ocean Stratification during Strong Diurnal SST Variation Events in the Suppressed Phase of the MJO

Je-Yuan Hsu[1], Ming Feng[2, 3] and Susan Wijffels[4]

[1]Institute of Oceanography, National Taiwan University, Taipei, Taiwan

[2]CSIRO Oceans and Atmosphere, Perth, Australia

[3]Centre for Southern Hemisphere Oceans Research (CSHOR), Hobart, Australia

[4]Woods Hole Oceanographic Institution, Woods Hole, USA

Corresponding Author: Je-Yuan Hsu

Email: jyahsu@ntu.edu.tw

February 1, 2021

Submitted to *Journal of Geophysical Research: Oceans*

Abstract

Six ALAMO floats are deployed within the tropical warm pool of the eastern Indian Ocean, to study the thermal stratification in the diurnal warm layer (DWL) during strong diurnal SST variation (DV SST) prior to the onset of Madden-Julian Oscillations (MJO). Strong DV SST of > 2 °C is measured by four floats before the passage of a MJO event (i.e., during the suppressed phase), when the peak insolation > 1000 W m^{-2} and the wind speed < 3 m s^{-1}. Even after the occurrence of daytime peak SST, the temperature gradient in the DWL can still extend to > 10 m until the midnight, which may be driven by the turbulent mixing at the base of DWL. Interestingly, the foundation SST (SST_{fnd}) at three floats increases rapidly from 26.4 °C to > 27.6 °C over two days, coincident with the shoaling of surface mixed layer depth (MLD) by more than 20 m. The strongly stratified near surface layer may sustain higher SSTs and enhance air-sea heat fluxes until the onset of stronger winds. The KPP mixing scheme used in a 1-D model can simulate the observed DV SST magnitude reliably, but fail to predict the rapid increase of SST_{fnd}. The magnitude of DV SST is affected by the near surface stratification, but the SST_{fnd} is modulated by the evolution of stratification above the MLD. Future field measurements in the upper ocean during diurnal warming are proposed to help improve air-sea flux simulations and the forecast of MJOs.

1. Introduction

Air-sea heat fluxes over high sea surface temperatures (SST) of the tropical warm pools (TWPs) have a critical influence on the atmospheric general circulation. These TWPs frequently feature low wind conditions and thus experience ubiquitous and strong diurnal variations of SST (DV SST). Latent and sensible heat fluxes, modulated by the SST, can affect the onset and timing of intra-seasonal weather systems such as the MJOs (Zhang 2005; Maloney 2009; Seo et al. 2014; Sobel et al. 2014). While the intrinsic time scale of MJOs is longer than a week, the coupled model forecasts of MJOs can be influenced significantly by DV SSTs through impacts on daily-mean SST (Bernie et al. 2008; Rupert and Johnson 2015; Demott et al. 2015). Modeling the diurnal variations of the upper ocean remains challenging (Kawai and Wada 2007). To forecast the DV SST accurately, turbulent mixing in the upper ocean must also be simulated accurately, which involves the forecast on both the shear and density stratification for inducing shear instability mixing. Therefore, exploring the diurnal SST variations and associated evolution of stratified layers near the ocean surface may be crucial for improving the MJO forecast.

The evolution of stratified layers (Fig. 1) above the seasonal thermocline during the DV SST has been discussed in several previous studies such as Brainerd and Gregg (1993a) and Sutherland et al. (2016). Under low wind conditions, the absorption of insolation during the daytime forms a sharp vertical temperature gradient in the surface mixed layer, termed the diurnal thermocline (Kudryavtsev and Soloviev 1990; Caldwell et al. 1997). The diurnal warm layer (DWL, Sui et al. 1997; Matthews et al. 2014; Sutherland et al. 2016; Moulin et al. 2018; Hughes et al. 2020), spanning the ocean surface to the base of diurnal thermocline, can modify the magnitude of DV SST through the inhibition of turbulent mixing across its base (Fairall et al.

1996b; Bellenger and Duvel 2009; Moulin et al. 2018). Below, the layer between the DWL and the top of the seasonal thermocline is termed the remnant layer (RL, Brainerd and Gregg 1993a; Caldwell et al. 1997), which can be regarded as a fossil mixed layer formed during the previous night due to convective cooling. The penetrative solar radiation can not only form the DWL, but also restratify the RL (Brainerd and Gregg 1993a). After a late afternoon peak, the SST drops around sunset when outgoing turbulent heat fluxes and longwave radiation exceed the insolation (Moulin et al. 2018), and thus induces nighttime convective mixing. The induced convective mixing will then mix the surface mixed layer by destratifying the DWL and RL (Fig. 1c). It will set the foundation SST (SST_{fnd}, which is closed to the nighttime minimum SST) similar with that of the previous night.

Consecutive days of strong insolation and low wind speeds is one of the most important features of the suppressed phase of MJO. This can result in the stratification of surface mixed layer (e.g., Bernie et al. 2005; Moum et al. 2014) and generate higher daily-mean SST (Shinoda and Hendon 1998; Bernie et al. 2005). The insolation captured in the DWL will be redistributed through the deeper surface mixed layer by nighttime convective mixing. This heat can gradually increase the SST_{fnd} and the stratification across the base of the DWL (Sui et al. 1997). In turn it may suppress cold entrainment, allow SSTs to increase and through associated air-sea fluxes, drive up the accumulation of atmospheric boundary layer heat and moisture for developing the deep convection in MJOs (Zhang and Ling 2017)

The concept of an ocean barrier layer (BL) is first proposed (Lukas and Lindstrom 1991) to identify the discrepancy between the surface mixed layer depth (MLD) and the top of seasonal thermocline, mostly due to opposing salinity stratification. The BL is later defined as the layer between the isothermal layer depth (ILD) and MLD (Sprintall and Tomczak 1992; McPhaden

and Foltz 2013; Chi et al. 2014). Strong precipitation may form a low-salinity layer near the sea surface (as illustrated in Fig. 1d and h). The density stratification due to salinity will result in a shallow MLD, while the temperature remains nearly homogenous (i.e., the definition of isothermal layer IL) or even can be cooler at the surface compared to below (McPhaden and Foltz 2013; Chi et al. 2014). The presence of salinity-based BL increases the required vertical mixing to access the seasonal thermocline (Chi et al. 2014). On the other hand, the temporal change of MLD is an useful indicator for identifying the strength of wind-driven mixing (Balaguru et al. 2015), because the nighttime convective mixing cannot destratify the temperature gradient in the seasonal thermocline abruptly. Thus, clearly salinity and temperature gradients in the upper ocean are important to the dynamics of stratification and turbulent mixing.

Though the importance of DWL for inhibiting the turbulent mixing has been explored by many previous studies (e.g., Moulin et al. 2018; Hughes et al. 2020), the thickness of DWL is often estimated by finding the depth of an isotherm with high temperature (Matthews et al. 2014). However, because the density stratification modulated by the temperature structure can affect the efficiency of turbulent mixing, exploring the factors to the extension of temperature "gradient" in the DWL should be more crucial than focusing on the thickness of a high-temperature layer. This study will discuss the evolution of temperature gradient above the MLD, by using both the observations and model simulations during a strong DV SST event.

In November 2018, a collaborative field campaign between CSHOR and China's First Institution of Oceanography was conducted to explore the air-sea interaction in the Indonesian-Australian Basin of the TWP (Feng et al. 2020). A shelf version of the Bailong buoy system (Appendix A) was deployed off the northwest coast of Australia, along with six rapidly profiling ALAMO floats from MRV Systems and two Teledyne Web EM-APEX floats. The observations

off Australia's Northwest Shelf collected during the suppressed phase of one MJO event around the end of 2018 (Feng et al. 2020) will be reviewed in section 2. Definitions and the estimation of different upper ocean stratified layers during diurnal warming will be described in section 3. Results and discussions on SST variations and evolution of upper ocean layers will be presented in sections 4 and 5, respectively. Section 6 will compare the observations with the model results using the K-profile parameterization (KPP) of vertical mixing.

2. ALAMO Float Measurements in the Field Experiment

The field array was deployed at 115.3 °E and 16.8 °S on Nov 22nd 2018. Two ALAMO floats (9206 and 9208) failed within two days of deployment. Floats 9205 and 9209 were deployed at the southwest of floats 9207 and 9210. The distance between the floats was always less than 50 km before Dec 5th. The remaining four ALAMO floats initially drifted northwestward (Fig. 2). The floats except 9205 turned east since Dec 2nd, but still remained in a cold filament whose SST ~ 26.5 °C. The drifting velocity of the floats is similar with the satellite-measured geostrophic current (not shown in this study). That is, the float trajectories should be mainly affected by the geostrophic currents of a strong cold-core cyclonic eddy located just east of the float array, not the wind-driven current. No rains fell until the passage of an MJO around the middle of December 2018 (Feng et al. 2020).

Two types of CTD sensors, Seabird SBE-41 (9207) and RBR (9205, 9206, 9208, 9209 and 9210), were mounted on the ALAMO floats. The floats continuously profiled the temperature and salinity in the upper 600 m from Dec 1st to 5th 2018. Only the ascending profiles are used for the analysis in this study, to avoid the CTD measurements being contaminated by

the wake effect. The time interval between ascending profiles was 3 to 4 h. The vertical resolution of Seabird profiles was 1 m in the upper 50 m. The RBR sensors returned a vertical resolution of 0.1 m in the upper 5 m, and 1 m from 5 to 50-m depth. We estimated the SST on the RBR profiles by finding the peak temperature in the upper 1 m, often at ~ 0.2-m depth, after excluding those with salinity measurements < 32 psu (which indicates air in the samples). ALAMO floats also recorded the temperature during surface drift, when the pressure was less than 0.2 dbar. Though the Seabird CTD sensors did not have the measurements in the upper 1 m, the first surface value of temperature at about 0.1 or 0.2 dbar was always several degrees higher than those reported at pressures < 0 dbar, similar with the typical difference between the air temperature and SST in the region. Thus, we used the first surface value of temperature on the Seabird surface reports as the SST at float 9207.

On Nov 28th 2018, the temperature in the upper 40 m at all four floats was about 26.3 °C and is largely vertically mixed until Dec 1st (Fig. 3). The float-measured SST was ~ 0.2 °C higher than the skin SST measured by the Himawari-8 satellites on Nov 30th (Fig. 2), consistent with previous studies (Beggs et al. 2013). The SST measurements taken by Himawari-8 satellites were described in appendix A. A strong DV SST event occurred between Dec 2nd and 4th (section 4), ~ 10 days before the passage of the deep convection in one MJO (often termed active phase; Feng et al. 2020) arrived in the region. Except for float 9205, the temperature in the upper 40 m increased up to 28 °C after Dec 3rd. Temperatures greater than 27 °C in the upper 40 m were then sustained until the onset of the MJO's active phase around Dec 13th. Float 9205 measured temperatures of > 26 °C down to 60-m depth on Dec 4th, deeper than that at the other three floats at 40-m depth, while the salinity in the upper 40 m at float 9205 was higher than that at the other floats by over 0.3 psu after Dec 2nd.

3. Definitions of Upper Ocean Stratified Layers and DV SST

Various criteria for estimating the depth of the MLD have been proposed (Sprintall and Roemmich 1999; de Boyer Montégut et al. 2004; Suga et al. 2004), such as a temperature difference that near the ocean surface (Wyrtki 1964) or density gradient criteria (Lukas and Lindstrom 1991). Some studies estimate the MLD by finding the difference of potential density $\Delta\rho$ between ρ(MLD) and $\rho(z_0)$ exceeding some arbitrary constant (e.g., $\Delta\rho = 0.1$ kg m^{-3} in Chi et al. 2014), where z_0 is the reference depth closed to the ocean surface. The definition of z_0 is required to exclude the unknown spikes of density gradient due to turbulence near the sea surface.

A key question is, which z_0 is shallow enough to represent the "surface" value of $\rho(z_0)$ (Brainerd and Gregg 1995)? Different studies choose z_0 to avoid the impact of diurnal near surface temperature stratification, e.g., $z_0 = 5$ m in McPhaden and Foltz (2013) or $z_0 = 10$ in de Boyer Montégut et al. (2004), due to either an interest in longer timescales or limited vertical observations. The daily development of temperature stratification in a DWL can complicate the estimates of MLD (as the example in Fig. 1f), conflicting with the simple concept of a persistent MLD at the top of seasonal thermocline. A more careful definition of z_0 needs to be used in the presence of a DWL.

3.1 Depth of stratified layers in a diurnal cycle

The absorption of insolation forms a DWL with strong temperature stratification in the surface mixed layer, developing within a few hours of sunrise (Moulin et al. 2018). Here, the diurnal warm layer depth is defined as the shallowest depth greater than 3 m (to avoid very near

surface turbulence) where vertical temperature gradients weaken to less than 0.02 °C m^{-1} over a 5-m span. That means temperature gradient is small below the DWL. This criterion focuses on illuminating the roles of strong near surface temperature gradients (including the diurnal thermocline) in stabilizing the upper ocean (Moulin et al. 2018), instead of the thickness of a high-temperature layer (e.g., Matthews et al. 2014; section 5). In other word, in this study, a "thicker" DWL occurs when a strong temperature gradient induced by the diurnal warming (> 0.02 °C m^{-1}) extends more deeply. The uncertainties of estimating DWL depth due to the choices of the values of temperature gradient and spanning depth are studied in supporting information A.

The MLD and ILD are estimated by using the estimated DWL as the reference depth z_0. We estimate the MLD by fulfilling two criteria at the same time: potential density difference $\Delta\rho = \rho(MLD) - \rho(z_0) > 0.15$ kg m^{-3} (McPhaden and Foltz 2013) and potential density gradient $\partial\rho/\partial z < -0.01$ kg m^{-4} (Brainerd and Gregg 1995), where the axis z is positive upward. The ILD is estimated in the same way as the MLD (Chi et al. 2014), but using the temperature-dependent profiles of ρ, which are computed assuming a constant salinity – here, the average of salinity in the upper 5 m.

3.2 Temperature versus salinity-driven BL

The barrier layer (BL) described by Lukas and Lindstrom (1991) exists due to salinity stratification for driving the discrepancy between the MLD and ILD (Fig. 1d and h. McPhaden and Foltz 2013; Chi et al. 2014). They also report a DWL near the ocean surface during the daytime. Because the strong temperature stratification in the DWL stabilizes the upper ocean, the effect of the DWL on vertical mixing (Moulin et al. 2018) can be similar to that of near surface

freshening (Smyth et al. 1997), and thus form a BL. Here, we will define a temperature-driven BL (TBL) and salinity-driven BL (SBL). The TBL is identified if DWL > 10 m. The SBL is identified if ILD – MLD > 15 m (see supporting information A for more details on the criteria).

Example profiles of salinity and temperature are used to illustrate the difference between TBL and SBL (Fig. 4). A sharp diurnal thermocline with a temperature gradient extending to > 20-m depth, i.e., a thick DWL, is captured by float 9210 in the afternoon on Dec 2nd. Strong density stratification in the TBL is due to the absorption of insolation. In comparison, at float 9209, the salinity stratification between 20 and 40-m depth around the 7am of Dec 3rd leads to the separation of the ILD and MLD, due to a shallower SBL. The TBL and SBL (Chi et al. 2014) driven by temperature and salinity stratification, respectively, may both increase the upper ocean stratification, and thereby the threshold for the shear needed to induce vertical mixing.

3.3 Magnitude of DV SST and foundation SST

The Group for High Resolution Sea Surface Temperature (GHRSST) defines the foundation SST (SST_{fnd}) as the SST not affected by the diurnal variability, or the SST before solar heat gain begins early in the day. Estimating the SST_{fnd} is difficult without using reliable measurements of air-sea heat fluxes or models for predicting diurnal variation (Zhang et al. 2016). Several studies find the SST_{fnd} by averaging the nighttime SSTs before sunrise - from 12 to 5:30 am (Karagali and Høyer 2014; Zhang et al. 2016). Following this, we define SST_{fnd} as the mean SST from 1 to 5 am. The magnitude of DV SST is then the difference between the SST_{fnd} and following peak SST (SST_{max}).

4. SST Warming and Air-sea Heat Fluxes

We compute the SST_{fnd} and the magnitude of DV SST from Dec 1st to 4th 2018 (section 3), by using the float measurements of SST. On Dec 1st, the observed SST_{fnd} at all floats is similar, ~ 26.4 °C, and reaches the peak (~ 26.9 °C) at around 3 - 4 pm. Compared with the magnitude of DV SST reported by the previous studies (e.g., from 0.5 to 1.3 °C in Moulin et al. 2018), the magnitude of DV SST ~ 0.5 °C on Dec 1st is not extremely high (Fig. 5b-e). From Dec 2nd to 3rd, the significant DV SST > 2 °C occurs at all floats, termed a strong DV SST event in this study. The highest SST of 29 °C occurs at the float 9209 on Dec 3rd.

Air-sea heat fluxes are computed (Fig. 6) using the atmospheric measurements from the surface buoy and float-measured SST (supporting information B), based on the COARE 3.0 algorithm (Fairall et al. 1996a; Fairall et al. 2003). The trend of daily-mean air-sea net heat flux is consistent with that of upper ocean heat storage rate. The latent (LH) plus sensible heat flux (SH) drops from 220 to 80 W m^{-2} between Dec 1st and 3rd, because the wind speed decreases down to 2 m s^{-1} (Fig. 5a). The peak of downward shortwave radiation before Dec 2nd is already > 900 W m^{-2} (appendix A), and low vertical shear of horizontal current is observed at the surrounding EM-APEX float (not shown in this study), presumably due to the low wind speed. That is, this strong DV SST event in the beginning of December mainly results from the decreasing wind speed since Dec 1st, not increasing insolation.

The warming of SST_{fnd} varies significantly between each float from Dec 2nd to 4th (Fig. 5), even when their separation is less than 50 km. The SST_{fnd} at floats 9207 and 9210 increases from 26.6 to 27.7 °C from Dec 2nd to 3rd in one day, right after the significant DV SST > 2 °C on Dec 2nd. The SST_{fnd} at float 9209 increases from 26.4 to 27.6 °C between Dec 2nd and 4th. The

244 SST_{fnd} at float 9205 is ~ 27 °C, smaller than the other three floats by 0.8 °C on Dec 4th. The
245 equivalent mean net heat flux at float 9205 is therefore ~ 8.4 W m^{-2} lower than that at the floats
246 9207 and 9210 from Dec 2nd to 4th (Fig. 6).
247 On the other hand, though the LH is suppressed by the low wind speed from Dec 2nd to
248 4th, the SST_{fnd} warming will eventually favor the LH once the wind speed increases (Hsu et al.
249 2019), e.g., the LH is up to -220 W m^{-2} at wind speed > 6 m s^{-1} on Dec 6th (not shown in this
250 study). The relative humidity rises to more than 80 % after Dec 7th as well (appendix A). In other
251 words, the warming of SST_{fnd} in a short time period may largely enhance the "efficiency" for
252 accumulating of air-sea heat fluxes and moisture during the suppressed phase of MJOs (Maloney
253 2009).
254

255 **5. Upper Ocean Stratified Layers during Strong DV SST**

256 ***5.1 Evolution of DWL***

257 The strength of the ocean stratification is tracked through computing the Brunt-Väisälä
258 frequency N^2 (=-(g/ρ)(∂ρ/∂z), where g is the gravity constant). The DWL is thin (< 10 m) on Dec
259 1st, associated with a small DV SST, ~ 0.5 °C. Starting from Dec 2nd, the solar insolation forms a
260 "thick" DWL as a TBL that extends its temperature gradient to more than 20-m depth, resulting
261 in strong density stratification ($N^2 > 1.0\times10^{-4}$ s^{-2}) near the ocean surface (Fig. 5). Note that the
262 criteria for estimating the DWL depend on only the temperature gradient. The extension of N^2
263 results from the vertical structure of temperature instead of salinity.
264 We further compare the estimates of DWL with the other definition of diurnal warm layer
265 DWL^* (with the superscript *) in the aspect of a high-temperature layer. The DWL^* can be found

at the depth of an isotherm in each day, whose temperature T^* equals to $\alpha*SST_{max} + (1-\alpha)SST_{fnd}$ or is at least 0.1 °C higher than the SST_{fnd}, assuming the $\alpha = 0.3$ (Matthews et al. 2014). Considering the variations of SST_{max} and SST_{fnd} between different days, the DWL^* can only be used for comparing with the DWL in the individual day. During the strong DV SST event (Fig. 7), both DWL and DWL^* reach the peak in the evening or at the midnight (after 7 pm each day), within several hours after the occurrence of SST_{max} in the afternoon (~4 pm each day; section 4). The turbulent diffusivity after the diurnal peak transports the warm water and extents the temperature gradient to the deeper layer until the midnight. The DWL can be a reliable indicator for identifying the strong DV SST in the consecutive days.

When the measured DV SST at all floats is > 2 °C (Fig. 5), not only a thin layer with high temperature is formed near the sea surface, a TBL with the significant extension of strong temperature gradient also appears in the upper ocean. Interestingly, even the thin and high-temperature (~ SST_{max}) layer within the upper 5 m disappears before 6 pm on Dec 3rd (Fig. 7), the extension of temperature gradient in the DWL is not shoaled to < 5 m until the midnight of Dec 4th. The deepening of DWL before the nighttime convective mixing may be induced by the shear at the base of DWL (Matthews et al. 2014; Hughes et al. 2020). Because the density stratification is affected by the temperature structure, the extension of temperature gradient driven by the vertical shear (Hughes et al. 2020) may nonlinearly affect the turbulent diffusivity above the MLD, and thereby the cooling of SST from the daytime peak.

5.2 Stratification above the MLD

The MLD is estimated by using the DWL as the reference depth to avoid the temperature gradient in the DWL (section 3). Because of the large N^2 below the MLD, the estimated MLD

captures the top of the seasonal thermocline reliably, ~ 50 m before Dec 2nd. Strong nighttime convective mixing occurs above the MLD ($N^2 < 0$ shaded by the white color in Fig. 5), mainly driven by latent heat flux and longwave cooling. During the strong DV SST event (section 4), the MLD at the floats except 9205 is shoaled by 20 m, consistent with the change of SST_{fnd} from 26.6 to > 27.7 °C. At float 9205, the MLD and SST_{fnd} are nearly constant. Because the salinity at float 9205 is higher than that at the other floats, we suspect that different vertical structure of salinity between the floats may be associated with the variation of MLD shoaling.

Because the trajectories of the floats are slightly different, the measured vertical structure of the salinity between the floats is not the same during the strong diurnal SST warming. On Dec 3rd, float 9209 measure a fresh-water layer with salinity ~34.4 psu near the sea surface. It results in a SBL at 30-m depth during the diurnal warming. Because the simulated magnitude of DV SST at float 9205 is still similar with the observation, the presence of SBL in the subsurface layer may not affect the DV SST significantly.

Except at float 9205, the average of N^2 between 20 and 40-m depth (part of the surface mixed layer on Dec 1st) increases from 5.0×10^{-5} to 1.0×10^{-4} s^{-2} from Dec 2nd to 4th. It shoals the MLD by > 20 m. The restratification rate $\partial N^2/\partial t$ is ~3.5×10^{-10} s^{-3}, much faster than that reported by Brainerd and Gregg (1993a) during the daytime (< 4 m s^{-1} and peak insolation ~ 700 W m^{-2}), ~ 1.6×10^{-10} s^{-3}. The upper ocean becomes stably stratified in a few days. More importantly, though the wind speed increases to > 6 m s^{-1} after Dec 5th, the MLD at floats 9207 and 9209 is still about 30 m, shallower than that at 50-m depth before Dec 2nd (Fig. 3). The decrease of MLD agrees with the increase of SST_{fnd} from 26.5 °C to > 27 °C before and after the strong DV SST event.

311 Clearly, the increase of SST_{fnd} is inversely proportional to the shoaling of MLD,
312 consistent with the model results reported by Bernie et al. (2005). The SST_{fnd} can be higher if the
313 same amount of heat content is accumulated in a shallower MLD. The shoaling of MLD also
314 coincidentally occurs after the strong DV SST > 2 ℃ except float 9205. Because the extension
315 of temperature gradient in the DWL can inhibit the vertical mixing efficiently, we speculate that
316 the thick DWL as a TBL may reduce the nighttime convective mixing for eroding the
317 stratification above the MLD. It prolongs the period for the penetrative solar radiation to
318 restratify the RL and shoal the MLD in the following day.
319 Despite of it, there may be some other factors for causing the restratification in the RL.
320 The role of penetrative solar radiation is studied in a one-dimensional model. The change of heat
321 absorption at different layers does not affect the density stratification below 30-m depth
322 significantly (section 6.2). The effect of horizontal advection is also studied. According to the
323 satellite measurements, the temperature advection at the sea surface may be insignificant near the
324 floats (supporting information C). However, without sufficient float measurements as direct
325 evidences, it is hard to quantify the temperature advection driven by the warm patch at 115 °E
326 and 15.3 °S (Fig. 2), and thereby the restratification of RL (Brainerd and Gregg 1993b). That is,
327 the cause of the rapid restratification of RL is still in doubt in this study. Understanding the
328 mechanism for changing the MLD is crucial for predicting the SST_{fnd} variations in the future.
329

330 **6. Simulations of SST Variations using the KPP mixing scheme**

331 The strong DV SST > 2 ℃ is observed at all ALAMO floats, associated with the
332 extension of temperature gradient in the DWL to the deeper layers (section 5). Can a numerical

model simulate the near surface temperature stratification we observed during these strong DV SST events accurately? More importantly, which factors may be crucial for simulating the upper ocean stratification during the diurnal warming? Compared with the multi-layer models such as PWP3D (Price et al. 1986), the K-profile parameterization (KPP) can better simulate the DV SST (Kawai and Wada 2007), and has been used in several ocean models (e.g., Shinoda and Hendon 1998; Bernie et al. 2005). We will use the KPP in a one-dimensional Regional Oceanic Modeling System (ROMS; Shchepetkin and McWilliams 2005) to simulate the evolution of upper ocean stratification at the ALAMO array. Details of model settings and parameters in KPP are described in appendix B.

6.1 Simulated SST and density stratification N^2

We compare the model, with a fine vertical resolution near the ocean surface (section 6.2), with the observations (Fig. 8a-d). On the first day of model simulations (Dec 1st), the KPP simulated the SST reliably, including the DV SST of 0.5 °C. The simulated N^2 near the sea surface is similar to that observed, as found in Bernie et al. (2005). After Dec 1st, the model still predicts the SST at float 9205 well, including the SST_{max} of 29 °C on Dec 3rd. At float 9209, the simulated SST agrees with the observed SST well until the midnight of Dec 4th, i.e., before the shoaling of MLD from 40 to 20-m depth. The model results of SST at floats 9207 and 9010 differ from the observations significantly since Dec 2nd, consistent with the timing of rapid restratification in the RL.

The simulated temperature and salinity are used to compute the N^2 for discussing the evolution of upper ocean stratified layers (Fig. 8). For the floats 9205 and 9209, which have the similar MLD with the observations before Dec 4th, the simulated magnitude of DV SST agrees

with the observed DV SST. The occurrence of strong DV SST mainly results from the air-sea heat fluxes in the one-dimensional process. Though the simulated SST_{max} at floats 9207 and 9210 can still be > 28 °C on Dec 3rd, different N^2 above the MLD thereby SST_{fnd} results in the discrepancy of SST between the model and observations. Even the KPP mixing scheme simulates the DV SST magnitude and a highly stratified layer near the sea surface reliably, the failure on predicting the stratification above MLD may affect the simulated SST_{fnd} thereby the SST_{max}.

On the other hand, compared with the observed DWL, the thickness of simulated DWL is all less than 10 m, thinner than the observations after Dec 1st (Fig. 8e-l). The simulated N^2 in the DWL ($> 1.0 \times 10^{-3}$ s^{-2}) is two times larger than the float measurements from 12 to 4 pm between Dec 2nd and 4th. Most heat with high temperature gradient is accumulated near the sea surface in the model, unlike the observed temperature gradient extending to the deeper layer. In other words, though the magnitude of DV SST is similar, the structure of DWL between the model results and observations can still differ significantly.

6.2 Effect of penetrative solar radiation on the RL's restratification

Considering the importance of penetrative solar radiation for inducing diurnal warming and restratifying the RL (Brainerd and Gregg 1993b), different coefficients based on five water types are used in the parameterization of penetrative solar radiation (Paulson and Simpson 1978; appendix B) during the model simulations (Fig. 9). The model results at float 9209 will be discussed, because the SST difference at float 9209 between the model results and observations is not significant until the warming of SST_{fnd} on Dec 4th. Before Dec 3rd, the DWL in the upper 5 m can be simulated by all model runs with different water types. The simulated magnitude of DV

SST is similar with the observation. On Dec 3rd, the simulation using the water type I forms a shallower DWL with higher N^2 than the other water types. Because only the water type I has the significant DV SST > 2 °C, the value of N^2 in the DWL may be the most dominant factor for simulating the magnitude of DV SST.

Interestingly, the model results using the water type II or III have faster SST_{fnd} warming from Dec 2nd to 4th (~ 0.7 °C) than those using other water types. Though their simulated N^2 in the DWL is smaller than that in water type I, the N^2 in the DWL is not completely destratified by the nighttime convective mixing since the midnight of Dec 3rd. The remaining N^2 in the water types II and III implies that the simulated nighttime convective mixing may entrain less cold water from the seasonal thermocline to the ocean surface than that in the water type I. That is, the extension of temperature gradient to the deeper layer may more efficiently inhibit the nighttime convective mixing in the model simulations. The evolution of upper ocean stratification, including both DWL and MLD, is important to the forecast on the SST variations.

6.3 Effects of vertical resolution in the upper ocean

Several previous studies discuss the importance for using the vertical resolution $\Delta z \leq 1$ m in the simulation of DV SST (e.g., Bernie et al. 2005; Hughes et al. 2020). It may be sometimes impractical to use the vertical resolution of 1 m in the entire ocean model for a climate forecast. The effect of vertical resolution in different depth ranges of the upper ocean is thus studied by using fine and coarse grids in the SST simulations, respectively, as detailed in Fig. 10a.

The difference of simulated SST_{max} (Fig. 10) between the fine and coarse grids is negligible during the weak DV SST (e.g., Dec 1st and 2nd), but significant during the strong DV SST (e.g., Dec 3rd). High vertical resolution in the upper 20 m may directly affect the

accumulated heat near the ocean surface for the SST warming, by simulating the detailed structure of N^2 in the DWL, especially during the strong DV SST. The simulated SST_{fnd} in the coarse grids is slightly warmer than that in the fine grids on Dec 4th, after the strong diurnal warming on Dec 3rd. The Δz from 20 and 60-m depth may affect the simulated nighttime convective mixing, and thereby the SST cooling from the daytime peak to the nighttime minimum. Therefore, the Δz in the upper 20 m and from 20 and 60-m depth has a different impact on the SST variation. The Δz in the upper 20 m may affect the simulated N^2 in the DWL and SST_{max} in the afternoon. The Δz from 20 and 60-m depth may affect the simulations of the nighttime convective mixing and SST_{fnd}.

6.4 Parameters in the KPP mixing scheme

Because the KPP run with a high vertical resolution near the ocean surface fails to predict the structure of DWL and rapid SST_{fnd} warming at three ALAMO floats (section 6.1), the values of the mixing parameters in the K_ρ parameterizations are explored to seek improvements on the simulations of SST_{fnd} at float 9209 (Fig. 11). We will discuss the parameters Ri_c and Ri_0 (appendix B), which directly affect the vertical diffusivity K_ρ within and below the OBL, respectively.

Compared to the simulation using the default setting of mixing parameters (Ri_c = 0.3 and Ri_0 = 0.7), decreasing the Ri_c from 0.3 to 0.1 (i.e., assuming the OBL is thinner) has negligible effects to the simulated SST. Changing the thickness of the OBL may not affect the simulated SST_{max} significantly, presumably due to the similar K_ρ below the OBL. On the other hand, decreasing Ri_0 from 0.7 to 0.3 (i.e., more difficult for inducing shear instability) increases the SST_{max} significantly, but has negligible effect on the SST_{fnd}. Inhibiting the vertical mixing by

restricting the depth range of K_ρ may affect the prediction of SST_{max}. If the Ri_0 alternatively increases from 0.7 to 1 (i.e., larger depth ranges of K_ρ to transport heat at the base of OBL), the KPP still fails to simulate the rapid SST_{fnd} warming. That is, the Ri_0 which affects the turbulent diffusivity below the DWL is the most important parameter for the simulated DV SST magnitude in the KPP.

7. Summary and Conclusion

Six ALAMO floats with high vertical resolution ≤ 1 m in the upper 50 m are deployed off the northwest Australia on Nov 22nd 2018. Four floats measure strong DV SST of up to 2 °C in the beginning of December, under low wind speed (~ 2 m s^{-1}) and sunny conditions. A rapid SST_{fnd} warming is observed at three floats (9207, 9209 and 9210), rising from 26.4 to more than 27.6 °C between Dec 2nd and 4th. The increase of SST_{fnd} at float 9205 is ~ 0.5 °C, lower than that at the other floats. The warming rate of SST_{fnd} varies significantly, even though the distance between floats is less than 50 km. Because of the rapid SST_{fnd} warming, the latent plus sensible heat flux at floats 9207 and 9210 is ~8.4 W m^{-2} higher than that at float 9205 from Dec 2nd to 4th.

To emphasize the presence of a strong temperature gradient above the surface mixed layer during the diurnal warming, a diurnal warm layer depth (DWL) is defined here by finding the mean temperature gradient $\partial T/\partial z$ from z_0 to (z_0+5)-m depth > 0.02 °C m^{-1}. In other word, a thick DWL will extend its strong temperature gradient to the deeper layer. Under the strong DV SST ~ 2 °C, the averaged N^2 within the thick DWL (~ 20 m) is more than 1.0×10^{-4} s^{-2}. Below the DWL, N^2 in the surface mixed layer increases from 5.0×10^{-5} to 1.0×10^{-4} from Dec 2nd to 4th. This restratification rate is faster than that reported by previous studies (e.g., Brainerd and

447 Gregg 1993a). This fast restratification below the DWL may prolong the period of high SST in
448 the tropical warm pool.

449 The KPP mixing scheme in a 1-D ROMS model is used to simulate the SST and upper
450 ocean stratified at the float positions. The simulated SST agrees well with the observed SST at
451 float 9205, including the strong DV SST > 2 °C. However, the model fails to simulate the rapid
452 SST_{fnd} warming at the other three floats, presumably due to the other factors for simulating the
453 restratification above the MLD. Factors impacting the simulation of SST variations in the KPP
454 are discussed. High vertical resolution in the upper 20 m of < 1 m is required for reliably
455 simulating the magnitude of DV SST. Decreasing the mixing parameter Ri_0 for inhibiting the
456 turbulent diffusivity in the diurnal thermocline can directly increase the peak SST in the model
457 simulations. Changing the mixing parameter Ri_c has negligible effects to the SST simulations.

458 In summary, a stable sunny atmosphere with low wind speed is favorable for the
459 formation of a thick DWL during the suppressed phase of the MJOs. The extension of
460 temperature gradient in the DWL is studied using the high vertical resolution measurements in
461 the first time, and can be more than 20 m during the strong DV SST > 2 °C. The shoaling of
462 MLD can also increase the SST_{fnd}. Though the KPP mixing scheme can simulate the DV SST
463 magnitude reliably by using high vertical resolution near the sea surface, it fails to predict the
464 increase SST_{fnd}, mainly due to different upper ocean density structure between the model and
465 observations. Questions still remain regarding to the factors for shoaling the observed MLD in a
466 short time period. Future field measurements on turbulent diffusivity within the DWL in TWPs
467 are important for improving the ocean mixing approaches in the global coupled models for the
468 MJO forecast.
469

Acknowledgments

This work is funded by the project of "Coupled warm pool dynamics in the Indo-Pacific" under the Centre for Southern Hemisphere Oceans Research (CSHOR). CSHOR is a joint initiative between the Qingdao National Laboratory for Marine Science and Technology (QNLM), CSIRO, University of New South Wales and University of Tasmania. The authors thank Dr. Beggs for advising the product of SST measured by the Himawari-8 satellite, the IMOS portal for processing the dataset of sea surface height anomalies in the dataset "IMOS - OceanCurrent - Gridded sea level anomaly - Delayed mode" (**https://portal.aodn.org.au/**), N. Bogue and R. Nigash at MRV for helping configure and pilot the floats, D. Slawinski (CSIRO) and P. Robbins (WHOI) for post-processing the float measurements. Float data is stored at **https://doi.org/10.25919/5da51c424add0**.

Appendix A. Buoy and Satellite Measurements

The Bailong buoy system from the First Institution of Oceanography (Cole et al. 2011) includes the atmospheric measurements near the ocean surface (Fig. 12) and subsurface ocean measurements in the upper 500 m (Feng et al. 2020). The atmosphere data is sampled in every 10 minutes. During the strong DV SST event from Dec 2nd to 4th 2018, the peak insolation is more than 1000 W m^{-2}, and the wind speed at 4-m height above the sea surface is about 2 m s^{-1}. Strong diurnal variation of air temperature is found, ~ 1 °C on Dec 2nd. The relative humidity (RH) is about 60%, and then increases until the onset of the MJO. The temporal variation of downward longwave radiation is small, from 400 to 450 W m^{-2}.

The infrared sensor mounted on the Japanese geostationary Himawari-8 satellite measures the skin SST in four spectral bands (8.59, 10.40, 11.24 and 12.38 μm) for every 10 minutes with the horizontal resolution < 2 km (Kramar et al., 2016). The product of Himawari-8 SST reprocessed by Dr. Christopher Griffin (http://opendap.bom.gov.au:8080/thredds/catalog/abom_imos_ghrsst_archive-1/v02.0fv03test/Continental/L3C-01hour/ABOM-L3C_GHRSST-SSTskin-AxIH08/2018/) in Bureau of Meteorology Australia as an hourly dataset is available online. We also use the near-real time sea surface height anomalies data processed by Integrated Marine Observing System (IMOS) data portal (Baird and Ridgway 2012; Deng et al. 2010), to understand the distribution of eddies around floats. The geostrophic current is computed, mostly northward and < 0.2 m s^{-1} along the trajectories of floats.

Appendix B. KPP Mixing Scheme in the 1-D ROMS Model Simulation

B.1. ROMS model description

The one-dimensional ROMS model with the KPP mixing is used to simulate the SST warming at each ALAMO floats. The atmosphere measurements taken by the FIO buoys, including insolation, downward longwave radiation, air temperature, air pressure, atmosphere wind and relative humidity, are used as the forcing at the floats, by assuming the spatial variation of atmosphere condition negligible within the distance of 80 km. The temporal resolution is 10 min. The profiles at each float from 9 to 11 pm on Nov 30th are averaged as the initial conditions.

We use the parameterization of penetrative solar radiation Q proposed by Paulson and Simpson (1977) for simulating the change of upper ocean stratification, which can be expressed as

$$Q = Q_0 \left(r \exp\left(\frac{z}{\mu_1}\right) + (1 - r) \exp\left(\frac{z}{\mu_2}\right) \right) \quad \text{(S2)}$$

where Q_0 is the insolation, r, μ_1 and μ_2 are the coefficients based on the data of five different water types in Jerlov (1976) (**Error! Reference source not found.**; https://www.myroms.org/wiki/Jwtype). According to the description in the ROMS model, water type I is used for open Pacific Ocean; water type IA is used for open Indian Ocean; water type IB is used for open Atlantic Ocean; water type II is used for Azores; water type III is used for North Sea. Most model results are simulated using the coefficients of water type I, except those in section 6.2.

B.2. KPP mixing scheme

The K-profile parameterization (KPP. Large et al. 1994) used in many ocean models, such as HYbrid Coordinate Ocean Model (HYCOM; Chassignet et al. 2007), computes the turbulent diffusivity by assuming a shape function in the OBL. It differs to the turbulence kinetic energy (TKE) closure scheme (e.g., Mellor and Yamada 1982), which uses a prognostic TKE energy equation and length scale of mixing.

In the KPP mixing scheme, after prescribing the surface forcing, the depth h of ocean boundary layer (OBL) will be first determined by using a critical bulk Richardson number Ri_c (default = 0.3). The diffusivity in the OBL, K_{Ric}, is computed based on the surface flux and h, assuming a nondimensional vertical shape function. For the diffusivity below the OBL, K_{Ri0}, the shear instability mixing occurs only when the local gradient Richardson number Ri is smaller than a critical gradient Richardson number Ri_0 (default = 0.7). The total diffusivity K_ρ is constituted by the K_{Ric}, K_{Ri0} and background diffusivity $K_{\rho 0}$ (default = 1.0×10^{-6}).

References

Baird, M. E., and K. R., Ridgway, 2012. The southward transport of sub-mesoscale lenses of Bass Strait Water in the centre of anti-cyclonic mesoscale eddies, Geophysical Research Letter, 39, L02603, doi:10.1029/2011GL050643.

Balaguru, K., G. R., Foltz, L. R. , Leung, E., D'Asaro, K. A. , Emanuel, H. , Liu, and S. E., Zedler, 2015. Dynamic Potential Intensity: An improved representation of the ocean's impact on tropical cyclones, Geophysical Research Letter, 42, 6739– 6746, doi:10.1002/2015GL064822.

Beggs, H., L., Majewski, G., Kruger, R., Verein, P., Oke, P., Sakov, X., Huang, L., Garde and C. Tingwell, 2013. Report to GHRSST14 from Australia — Bluelink and IMOS. **http://imos.org.au/fileadmin/user_upload/shared/SRS/Beggs_Australian_Report_GHRSST14_10Dec2013.pdf**

Bellenger, H. and J. Duvel, 2009. An Analysis of Tropical Ocean Diurnal Warm Layers. J. Climate. 22, 3629–3646. **https://doi.org/10.1175/2008JCLI2598.1**

Bernie, D. J., S. J. Woolnough, J. M. Slingo, and E. Guilyardi, 2005. Modeling Diurnal and Intraseasonal Variability of the Ocean Mixed Layer, Journal of Climate, 18, 1190-1202.

Bernie, D. J., E. Guilyardi, G. Madec, J. M. Slingo, S. J. Woolnough and J. Cole, 2008. Impact of resolving the diurnal cycle in an ocean–atmosphere GCM. Part 2: A diurnally coupled CGCM. Climate Dynamics, 31, 909-925, doi: 10.1007/s00382-008-0429-z

Brainerd, K. E. and M. C. Gregg, 1993a. Diurnal restratification and turbulence in the oceanic surface mixed layer: 1. Observations. Journal of Geophysical Research: Oceans, 98, 22645-22656, doi:10.1029/93JC02297.

564 Brainerd, K. E., and M. C. Gregg, 1993b. Diurnal restratification and turbulence in the oceanic
565 surface mixed layer: 2. Modeling, Journal of Geophysical Research, 98, 22657– 22664,
566 doi:10.1029/93JC02298.
567 Brainerd, K. E., and M. C. Gregg, 1995. Surface mixed and mixing layer depths, Deep Sea
568 Research Part I: Oceanographic Research Papers, 42, 1521-1543.
569 Caldwell, D. R., R-C. Lien, J. N. Moum, and M. C. Gregg, 1997. Turbulence decay and
570 restratification in the equatorial ocean surface layer following nighttime convection. Journal
571 of Physical Oceanography, 27, 1120–1132.
572 Chassignet, E. P., H. E., Hurlburt, O. M., Smedstad, G. R., Halliwell, P. J., Hogan, A. J.,
573 Wallcraft, R., Baraille and R., Bleck, 2007. The HYCOM (HYbrid Coordinate Ocean
574 Model) data assimilative system. Journal of Marine Systems 65, pp. 60-83. doi:
575 https://doi.org/10.1016/j.jmarsys.2005.09.016
576 Chi, N.-H., R.-C. Lien, E. A. D'Asaro and B. B. Ma, 2014. The surface mixed layer heat budget
577 from mooring observations in the central Indian Ocean during Madden–Julian Oscillation
578 events. Journal of Geophysical Research: Oceans. 119, 4638– 4652,
579 doi:10.1002/2014JC010192.
580 Cole, R., J. Kinder, Chun Lin Ning, W. Yu and Yang Chao, "“Bai-Long”: A TAO-hybrid on
581 RAMA," OCEANS'11 MTS/IEEE KONA, Waikoloa, HI, 2011, pp. 1-10. doi:
582 10.23919/OCEANS.2011.6106952
583 Cronin, M. F., and McPhaden, M. J., 1998. Upper ocean salinity balance in the western
584 equatorial Pacific, Journal of Geophysical Research, 103, 27567– 27587,
585 doi:10.1029/98JC02605.

de Boyer Montégut, C., G., Madec, A. S., Fischer, A., Lazar, and D. Iudicone, 2004. Mixed layer depth over the global ocean: An examination of profile data and a profile-based climatology, Journal of Geophysical Research, 109, C12003, doi:10.1029/2004JC002378.

DeMott, C. A., N. P. Klingaman, and S. J. Woolnough, 2015. Atmosphere-ocean coupled processes in the Madden-Julian oscillation, Reviews of Geophysics, 53, 1099-1154.

Deng, X, D. A. Griffin, K. Ridgway, J.A. Church, W.E. Featherstone, N. White and M. Cahill, 2010. Satellite altimetry for geodetic, oceanographic and climate studies in the Australian region, in: Vignudelli S., A. Kostianoy, and P. Cipollini and J. Benveniste (eds.), Coastal Altimetry, Springer-Verlag, Berlin. ISBN: 978-3-642-12795-3. e-ISBN: 978-3-642-12796-0. doi: 10.1007/978-3-642-12796-0_18

Drushka, K., S. T. Gille and J. Sprintall, 2014. The diurnal salinity cycle in the tropics. Journal of Geophysical Research: Oceans, 119, 5874-5890, doi: 10.1002/2014jc009924

Drushka, K., W., Asher, A., Jessup, E., Thompson, S., Iyer, D., Clark, 2019. Capturing Fresh Layers with the Surface Salinity Profiler. Oceanography. 32. 76-85. 10.5670/oceanog.2019.215.

Fairall, C. W., E. F., Bradley, D. P., Rogers, J. B., Edson, and G. S., Young, 1996a. Bulk parameterization of air-sea fluxes for Tropical Ocean-Global Atmosphere Coupled-Ocean Atmosphere Response Experiment, Journal of Geophysical Research, 101, 3747– 3764, doi:10.1029/95JC03205.

Fairall, C. W., E. F., Bradley, J. S., Godfrey, G. A., Wick, J. B., Edson, and G. S. Young, 1996b. Cool-skin and warm-layer effects on sea surface temperature, J. Geophys. Res., 101, 1295–1308, doi:10.1029/95JC03190.

608 Fairall, C.W., E. F. Bradley, J. E. Hare, A. A. Grachev, and J. B. Edson, 2003. Bulk
609 Parameterization of Air-Sea Fluxes: Updates and Verification for the COARE Algorithm. J.
610 Climate, 16, pp 571-591.
611 Feng, M., Y., Duan, S., Wijffels, J.-Y., Hsu, C., Li, H., Wang, Y., Yang, H., Shen, J., Liu, C.,
612 Ning, and W., Yu, 2020. Tracking air-sea exchange and upper ocean variability in the
613 Southeast Indian Ocean during the onset of the 2018-19 Australian summer monsoon.
614 Bulletin of the American Meteorological Society. https://doi.org/10.1175/BAMS-D-19-
615 0278.1.
616 Gargett, A. E., and G. Holloway, 1984. Dissipation and diffusion by internal wave breaking,
617 Journal of Marine Research, **42**, 15-27
618 Guilyardi, E., 2006. El niño-mean state-seasonal cycle interactions in a multi-model ensemble.
619 Climate Dynamics. 26. 329–348
620 Hsu, J.-Y., H., Hendon, M., Feng, and X., Zhou, 2019. Magnitude and phase of diurnal SST
621 variations in the ACCESS-S1 model during the suppressed phase of the MJOs. Journal of
622 Geophysical Research: Oceans, 124, 9553– 9571. https://doi.org/10.1029/2019JC015458
623 Hughes, K. G., J. N. Moum and E. L. Shroyer, 2020. Evolution of the Velocity Structure in the
624 Diurnal Warm Layer. Journal of Physical Oceanography, 50, 615-631, doi: 10.1175/jpo-d-
625 19-0207.1
626 Jerlov, N. G., 1976. Marine Optics, 14, Elsevier Oceanography Series
627 Karagali, I., and Høyer, J. L., 2014. Characterisation and quantification of regional diurnal SST
628 cycles from SEVIRI. Ocean Science, 10, 745–758. http://dx.doi.org/10.5194/os- 10-745-
629 2014.

630 Kawai, Y. and Wada, A., 2007. Diurnal sea surface temperature variation and its impact on the
631 atmosphere and ocean: A review. Journal of Oceanography, 63, 721-744, doi:
632 10.1007/s10872-007-0063-0
633 Kramar, M., A. Ignatov, B. Petrenko, Y. Kihai, P. Dash, 2016. Near real time SST retrievals
634 from Himawari-8 at NOAA using ACSPO system. Proc. SPIE 9827, Ocean Sensing and
635 Monitoring.
636 Kudryavtsev, V.N. and A.V. Soloviev, 1990. Slippery Near-Surface Layer of the Ocean Arising
637 Due to Daytime Solar Heating. Journal of Physical Oceanography, 20, 617–628,
638 https://doi.org/10.1175/1520-0485(1990)020<0617:SNSLOT>2.0.CO;2
639 Kunze, E., 2003. A review of oceanic salt-fingering theory. Progress in Oceanography, 56, 399-
640 417. doi: https://doi.org/10.1016/S0079-6611(03)00027-2
641 Large, W. G., J. C. McWilliams, and S. C. Doney, 1994. Oceanic vertical mixing: A review and
642 a model with a nonlocal boundary layer parameterization, Reviews of Geophysics, 32, 363-
643 403.
644 Lee, C., K.-I., Chang, J. H., Lee, and K. J., Richards, 2014. Vertical mixing due to double
645 diffusion in the tropical western Pacific, Geophysical Research Letter, 41, 7964– 7970,
646 doi:10.1002/2014GL061698.
647 Lukas, R., and E. Lindstrom, 1991. The mixed layer of the western equatorial Pacific Ocean, J.
648 Geophys. Res., 96(S01), 3343– 3357, doi:10.1029/90JC01951.
649 Maloney, E. D., 2009. The Moist Static Energy Budget of a Composite Tropical Intraseasonal
650 Oscillation in a Climate Model, Journal of Climate, 22, 711-729.

651 Matthews, A.J., D.B. Baranowski, K.J. Heywood, P.J. Flatau, and S. Schmidtko, 2014. The
652 Surface Diurnal Warm Layer in the Indian Ocean during CINDY/DYNAMO. Journal of
653 Climate, 27, 9101–9122, https://doi.org/10.1175/JCLI-D-14-00222.1
654 McPhaden, M. J. and G. R. Foltz, 2013. Intraseasonal variations in the surface layer heat balance
655 of the central equatorial Indian Ocean: The importance of zonal advection and vertical
656 mixing. Geophysical Research Letters. 40, 2737– 2741, doi:10.1002/grl.50536.
657 Mellor, G. L., and T. Yamada, 1982. Development of a turbulence closure model for geophysical
658 fluid problems, Rev. Geophys., 20, 851– 875, doi:10.1029/RG020i004p00851.
659 Moulin, A. J., J. N. Moum and E. L. Shroyer, 2018. Evolution of Turbulence in the Diurnal
660 Warm Layer. Journal of Physical Oceanography, 48, 383-396, doi: 10.1175/jpo-d-17-0170.1
661 Moum, J. N., S. P. de Szoeke, W. D. Smyth, J. B. Edson, H. L. DeWitt, A. J. Moulin, E. J.
662 Thompson, C.J. Zappa, S. A. Rutledge, R. H. Johnson, and C. W. Fairall, 2014. Air–Sea
663 Interactions from Westerly Wind Bursts During the November 2011 MJO in the Indian
664 Ocean. Bull. Amer. Meteor. Soc., 95, 1185–1199, https://doi.org/10.1175/BAMS-D-12-
665 00225.1
666 Paulson, C. A., and J. J. Simpson, 1977. Irradiance measurements in the upper ocean, Journal of
667 Physical Oceanography, 7, 952-956.
668 Price, J. F., R. A. Weller and R. Pinkel, 1986. Diurnal cycling: Observations and models of the
669 upper ocean response to diurnal heating, cooling, and wind mixing. Journal of Geophysical
670 Research: Oceans, 91, 8411-8427, doi: 10.1029/JC091iC07p08411
671 Ruppert, J. H., and R. H. Johnson, 2015. Diurnally modulated cumulus moistening in the
672 preonset stage of the Madden-Julian oscillation during DYNAMO, Journal of the
673 Atmospheric Sciences, 72, 1622–1647.

674 Seo, H., A. C. Subramanian, A. J. Miller, and N. R. Cavanaugh, 2014. Coupled Impacts of the
675 Diurnal Cycle of Sea Surface Temperature on the Madden–Julian Oscillation, Journal of
676 Climate, 27, 8422-8443, https://doi.org/10.1175/JCLI-D-14-00141.1
677 Shchepetkin, A. F., and J. C. McWilliams, 2005. The regional oceanic modeling system (ROMS)
678 a split-explicit, free-surface, topography-following-coordinate oceanic model. Ocean
679 Modelling, 9, pp. 347-404.
680 Shinoda, T. and H. H. Hendon, 1998. Mixed Layer Modeling of Intraseasonal Variability in the
681 Tropical Western Pacific and Indian Oceans. Journal of Climate, 11, 2668–2685,
682 https://doi.org/10.1175/1520-0442(1998)011<2668:MLMOIV>2.0.CO;2
683 Shinoda, T., T. G. Jensen, M. Flatau, and S. Chen, 2013. Surface Wind and Upper-Ocean
684 Variability Associated with the Madden–Julian Oscillation Simulated by the Coupled
685 Ocean–Atmosphere Mesoscale Prediction System (COAMPS), Monthly Weather Review,
686 141, 2290-2307.
687 Sobel, A., S. Wang, and D. Kim, 2014. Moist Static Energy Budget of the MJO during
688 DYNAMO, Journal of the Atmospheric Sciences, 71, 4276-4291.
689 Soloviev, A., and R., Lukas, 2006. The near-surface layer of the Ocean. Springer.
690 Sprintall, J., and M. Tomczak, 1992. Evidence of the barrier layer in the surface layer of the
691 tropics, J. Geophys. Res., 97, 7305– 7316, doi:10.1029/92JC00407.
692 Sprintall, J., and D. Roemmich, 1999. Characterizing the structure of the surface layer in the
693 Pacific Ocean, J. Geophys. Res., 104, 23,297–23,311.
694 Suga, T., K. Motoki, Y. Aoki, and A. M. Macdonald, 2004. The North Pacific climatology of
695 winter mixed layer and mode waters, Journal of Physical Oceanography, 34, 3–22.

696 Sui, C., X. Li, K. Lau, and D. Adamec, 1997. Multiscale Air–Sea Interactions during TOGA
697 COARE. Monthly Weather Review, 125, 448–462, https://doi.org/10.1175/1520-
698 0493(1997)125<0448:MASIDT>2.0.CO;2
699 Sutherland, G., L. Marié, G. Reverdin, K.H. Christensen, G. Broström, and B. Ward, 2016.
700 Enhanced Turbulence Associated with the Diurnal Jet in the Ocean Surface Boundary
701 Layer. Journal of Physical Oceanography, 46, 3051–3067, https://doi.org/10.1175/JPO-D-
702 15-0172.1
703 Vijith, V., P. N. Vinayachandran, B. G. M. Webber, A. J. Matthews, J. V. George, V. K.
704 Kannaujia, A. A. Lotliker and P. Amol, 2020. Closing the sea surface mixed layer
705 temperature budget from in situ observations alone: Operation Advection during BoBBLE.
706 Scientific Reports, 10, pp. 7062, doi: https://doi.org/10.1038/s41598-020-63320-0
707 Wyrtki, K., 1964. The thermal structure of the eastern Pacific Ocean, Deutsche hydrographische
708 Zeitschrift, 8, 6-84
709 Zhang, C., 2005. Madden-Julian Oscillation, Reviews of Geophysics, 43, RG2003,
710 doi:10.1029/2004RG000158.
711 Zhang, H., H. Beggs, L. Majewski, X. H. Wang, and A. Kiss, 2016. Investigating sea surface
712 temperature diurnal variation over the Tropical Warm Pool using MTSAT-1R data, Remote
713 Sensing of Environment, 183, 1-12.
714 Zhang, C. and J. Ling, 2017. Barrier Effect of the Indo-Pacific Maritime Continent on the MJO:
715 Perspectives from Tracking MJO Precipitation. Journal of Climate, 30, 3439–3459,
716 https://doi.org/10.1175/JCLI-D-16-0614.1
717 Zhao, Z., 2018. The global mode-2 M2 internal tide. Journal of Geophysical Research: Oceans,
718 123, 7725–7746. https://doi.org/10.1029/2018JC014475

719

720

721

722

723

Table

	Water Types				
	I	IA	IB	II	III
r	0.58	0.62	0.67	0.77	0.78
μ_1	0.35	0.60	1.00	1.50	1.40
μ_2	23.00	20.00	17.00	14.00	7.90

Table. 1. The coefficients used in the parameterization of penetrative solar radiation (Eq. S2) based on the data of five different water types reported by Jerlov (1976).

Figure

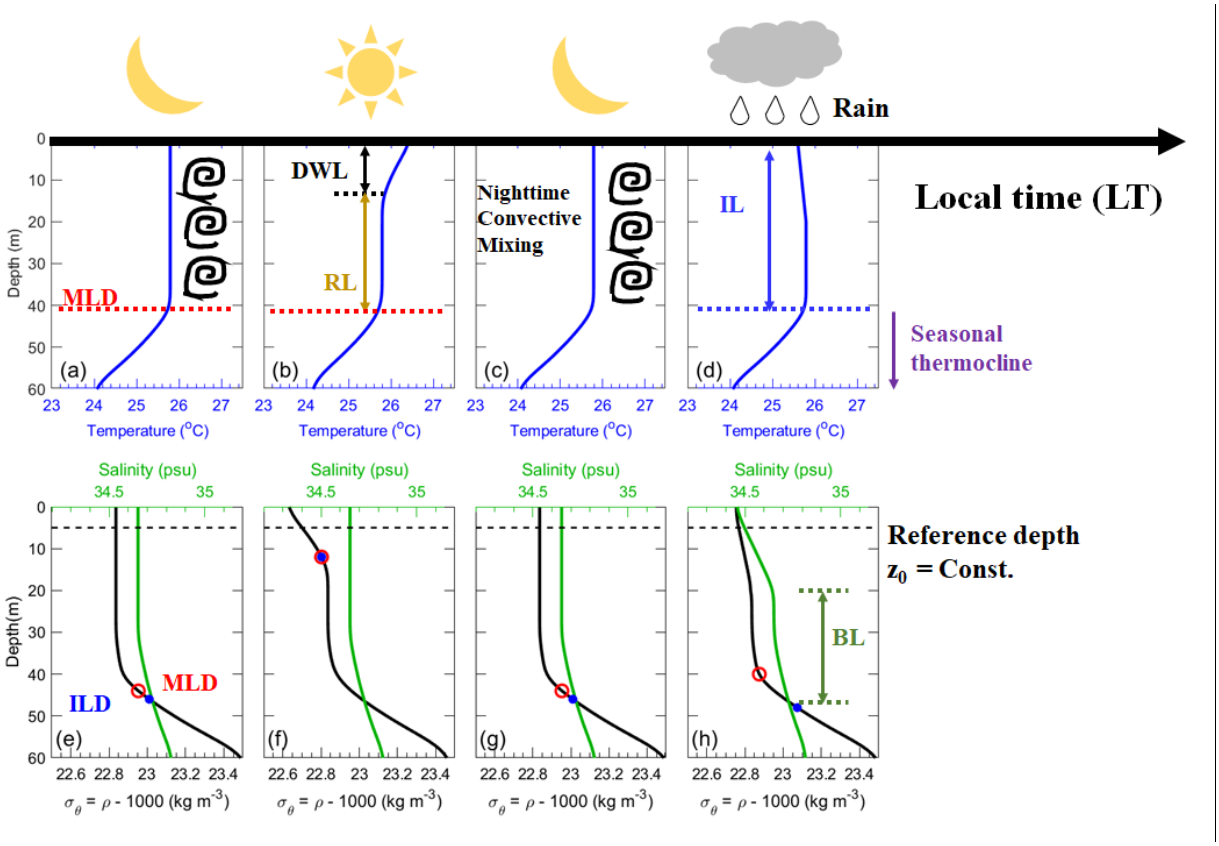

Fig. 1. Illustration on the surface mixed layer depth (MLD), diurnal warm layer (DWL), remnant layer (RL), isothermal layer (IL) and barrier layer (BL), using assumed temperature (blue lines in a-d) and salinity profiles (green lines in e-h). The RL exists between the DWL and MLD. Examples of estimating MLD and ILD based on the criteria used in the previous studies are presented in (e)-(h). The MLD (red circles) is estimated when the potential density difference $\rho(MLD) - \rho(z_0) > 0.1$ kg m^{-3} (Chi et al. 2014), assuming the constant reference depth z_0 at 5-m depth (black dashed lines in e-h). The isothermal layer depth (ILD. Blue dots) is estimated in the same way as the MLD but using temperature-dependent profiles of ρ, which assumes the salinity as the mean in the upper 5-m ocean. The formation of BL (difference between MLD and ILD > 20 m) is due to the precipitation freshening the salinity in the upper 20 m, and is regarded as the

742 salinity-driven barrier layer (SBL) in section 3. The temperature near the sea surface in (d) is
743 slightly cooled by rains (Druksha et al. 2019).

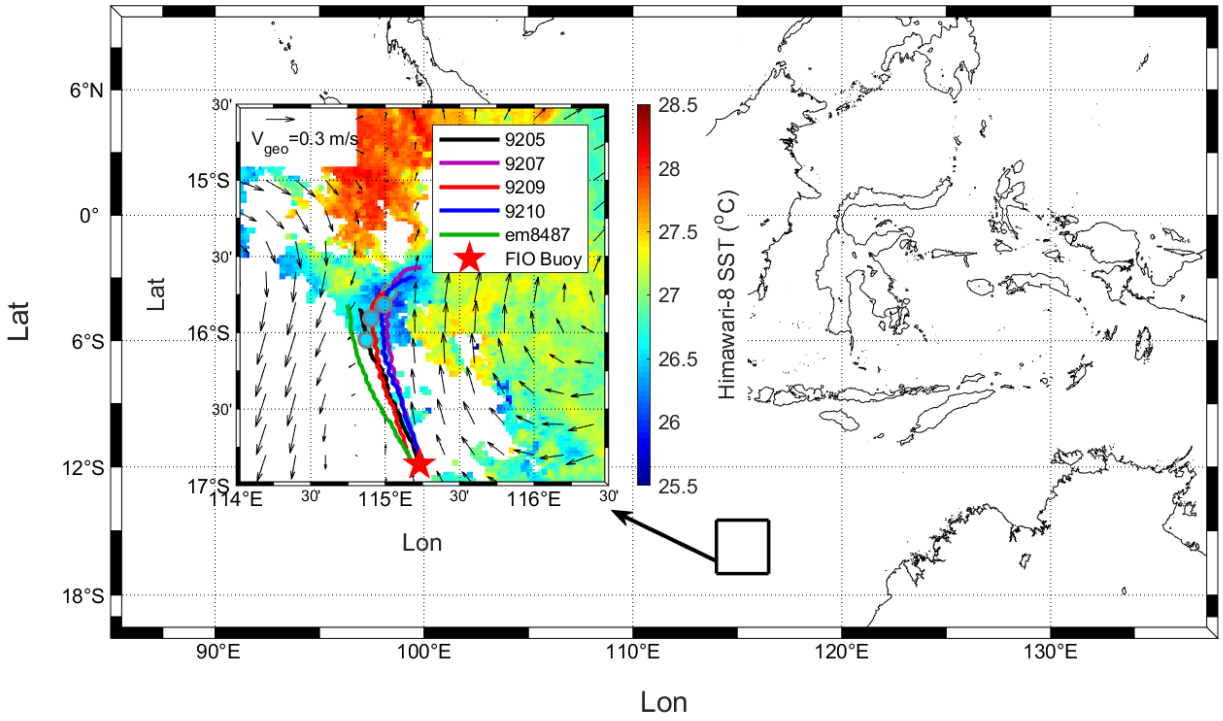

744

745 Fig. 2. Trajectories of four ALAMO floats (color lines) and one EM-APEX float (green line) in
746 the map of SST (color shading) measured by Himawari-8 satellite (appendix A) within the region
747 of TWP (black box in the big map) around 12 am on Dec 1st 2018. The ALAMO floats and EM-
748 APEX floats were deployed near the FIO buoy (red pentagram) at 115.3 °E and 16.8 °S in the
749 northwest Australia on Nov 22nd, and drifting northwestward (color lines are trajectories from
750 Nov 22nd to Dec 6th 2018) due to the geostrophic current (black arrows in the small map, and
751 their magnitude can be referenced to that on the upper-left corner). The color dots connected to
752 the ALAMO float trajectories are the float-measured SST around the midnight of Dec 1st 2018.
753 The geostrophic current V_{geo} is estimated using the IMOS sea surface heigth anomalies on Dec
754 1st 2018 (appendix A).

755

756

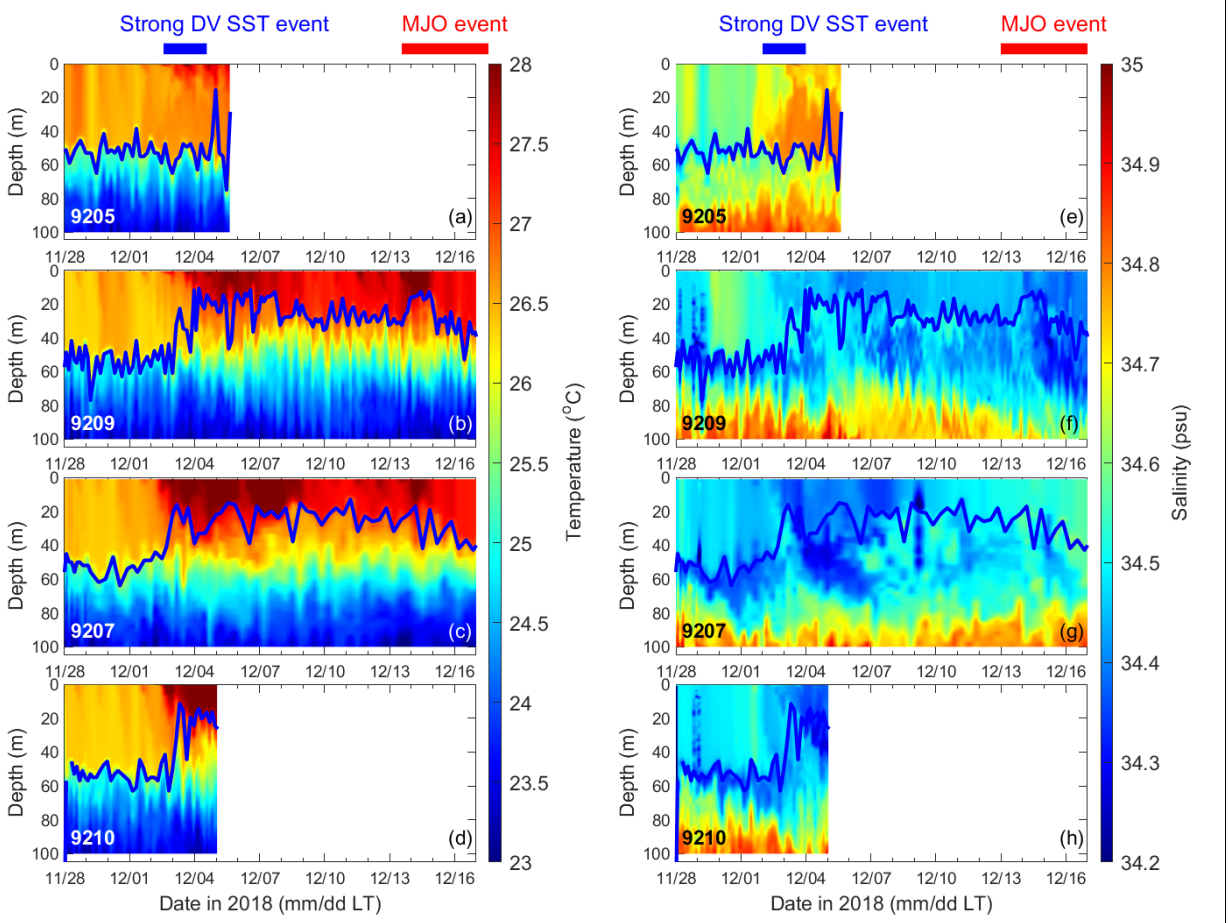

Fig. 3. Measurements of temperature (a-d) and salinity (e-h) in the upper 100 m taken by four ALAMO floats (9205, 9209, 9207 and 9210). The period of strong DV SST and MJO events are described in Feng et al. (2020). Blue lines are the estimated MLD (section 3).

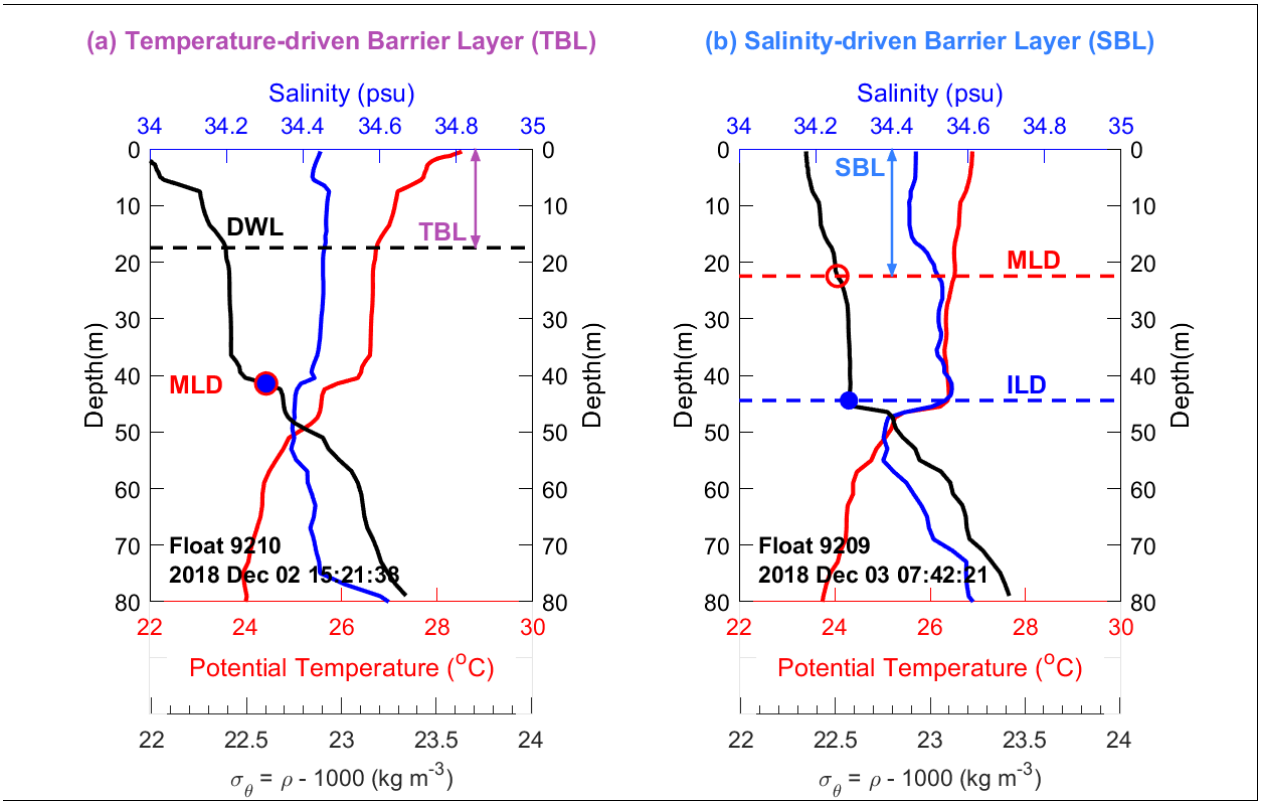

Fig. 4. Examples of temperature-driven barrier layer TBL (depth range indicated by the purple double arrow in a) and salinity-driven barrier layer SBL (depth range indicated by the light blue double arrow in b) based on the profiles of potential density anomaly σ_θ (= ρ-1000; black lines), potential temperature (blue lines) and salinity (red lines) at floats 9210 and 9209. The surface mixed layer depth MLD (red circles and red dashed line), isothermal layer depth ILD (blue dots and blue dashed line) and diurnal warm layer depth DWL (black dashed line) are estimated. The TBL is identified if DWL > 10 m. The SBL is identified if ILD – MLD > 10 m. More discussions on the criteria for identifying TBL and SBL can be found in supporting information A.

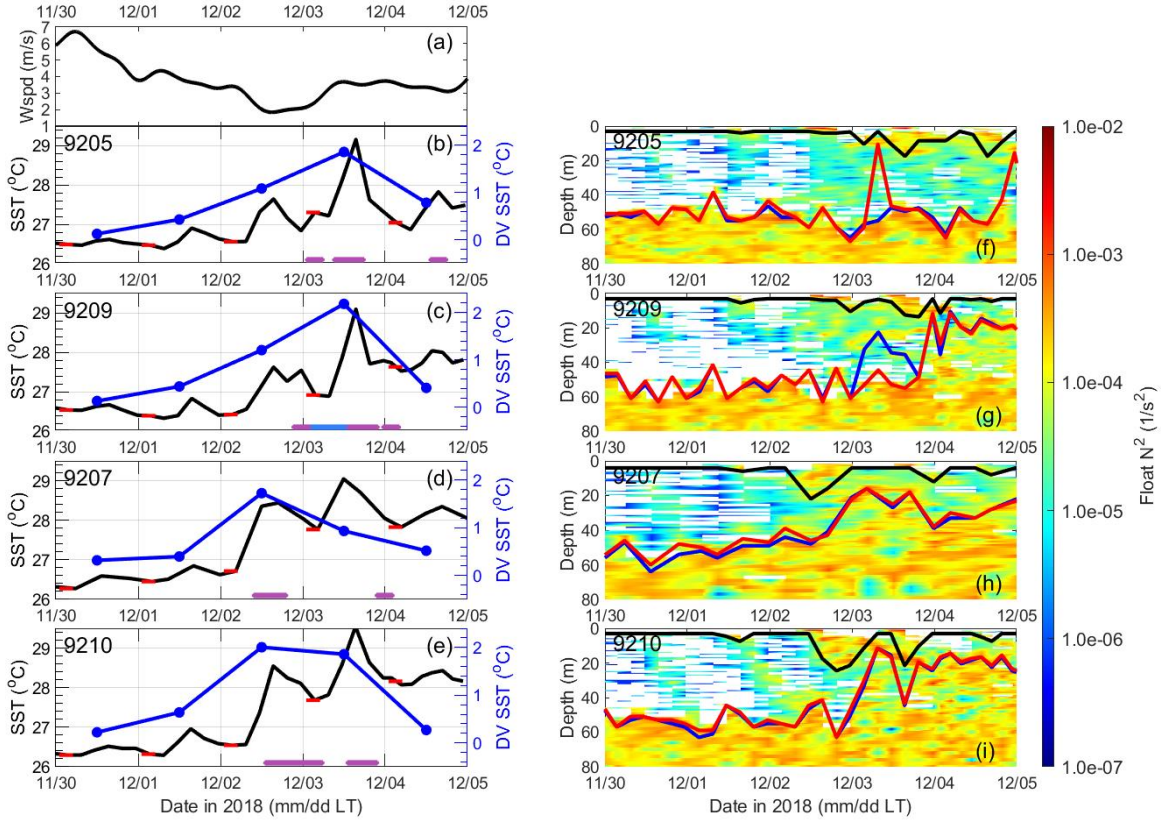

Fig. 5. Wind speed measurements on the buoy (a), and measurements of SST (black lines in b-e; referenced to the left axis), DV SST (blue dots connected with lines in b-e; referenced to the right axis) and N^2 (f-i; $N^2 < 0$ is shaded in white color) on four ALAMO floats (9205, 9207, 9209 and 9210). In (b)-(e), the red lines mark the foundation SST (SST_{fnd}; referenced to the left axis) in each day, and the purple and light blue bars in (b)-(e) mark the period where TBL and SBL exist, respectively. The TBL and SBL are identified using the estimates of DWL (black lines), MLD (blue lines) and ILD (red lines) in (f)-(i).

789

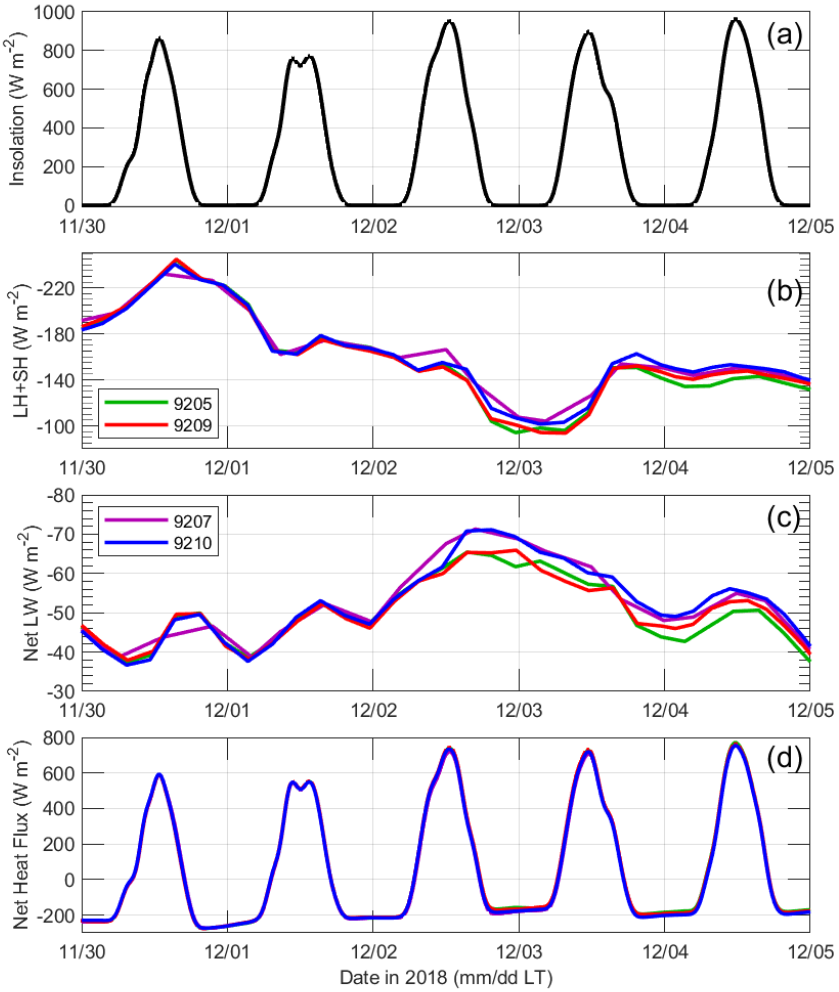

790

791 Fig. 6. Measurements of insolation on the buoy (a), and estimates of latent plus sensible heat flux

792 (b), net longwave radiation (c) and air-sea net heat flux (d) at four ALAMO floats (color lines).

793

794

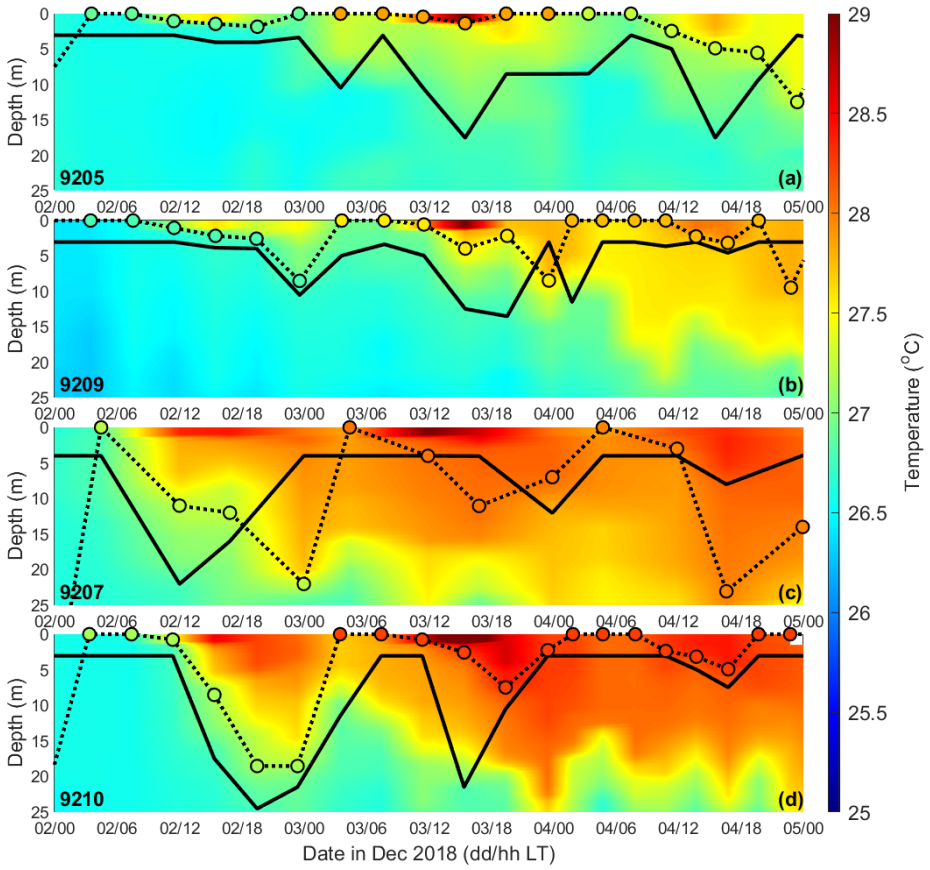

795

796 Fig. 7. Measurements of temperature (color shading) in the upper 25 m, estimated DWL (black

797 lines) and estimated DWL* (black dashed line connected with color dots) from Dec 2nd to 4th

798 2018 at four ALAMO floats (a-d). The color dots are the temperature T* of the isotherm, used for

799 finding the DWL*.

800

801

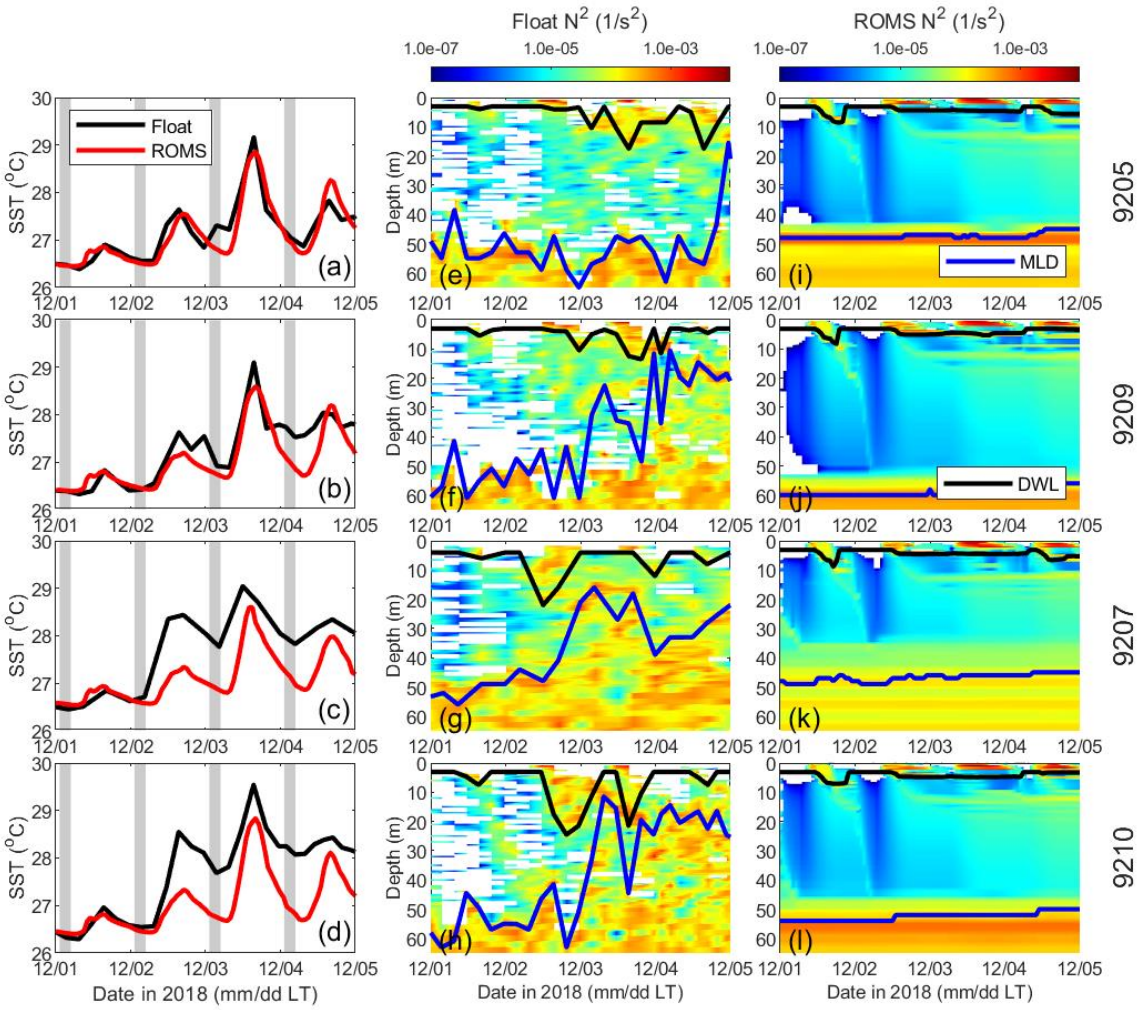

Fig. 8. Simulations of SST (red lines in a-d) and N^2 (color shading in i-l) using the KPP in the ROMS, compared with the observations of SST (black lines in a-d) and N^2 (color shading in e-h) at all ALAMO floats (each row). The period for computing the SST_{fnd} in each day is marked by the grey area in (a)-(d). The DWL (black lines) and MLD (blue lines) are estimated in (e)-(l), respectively.

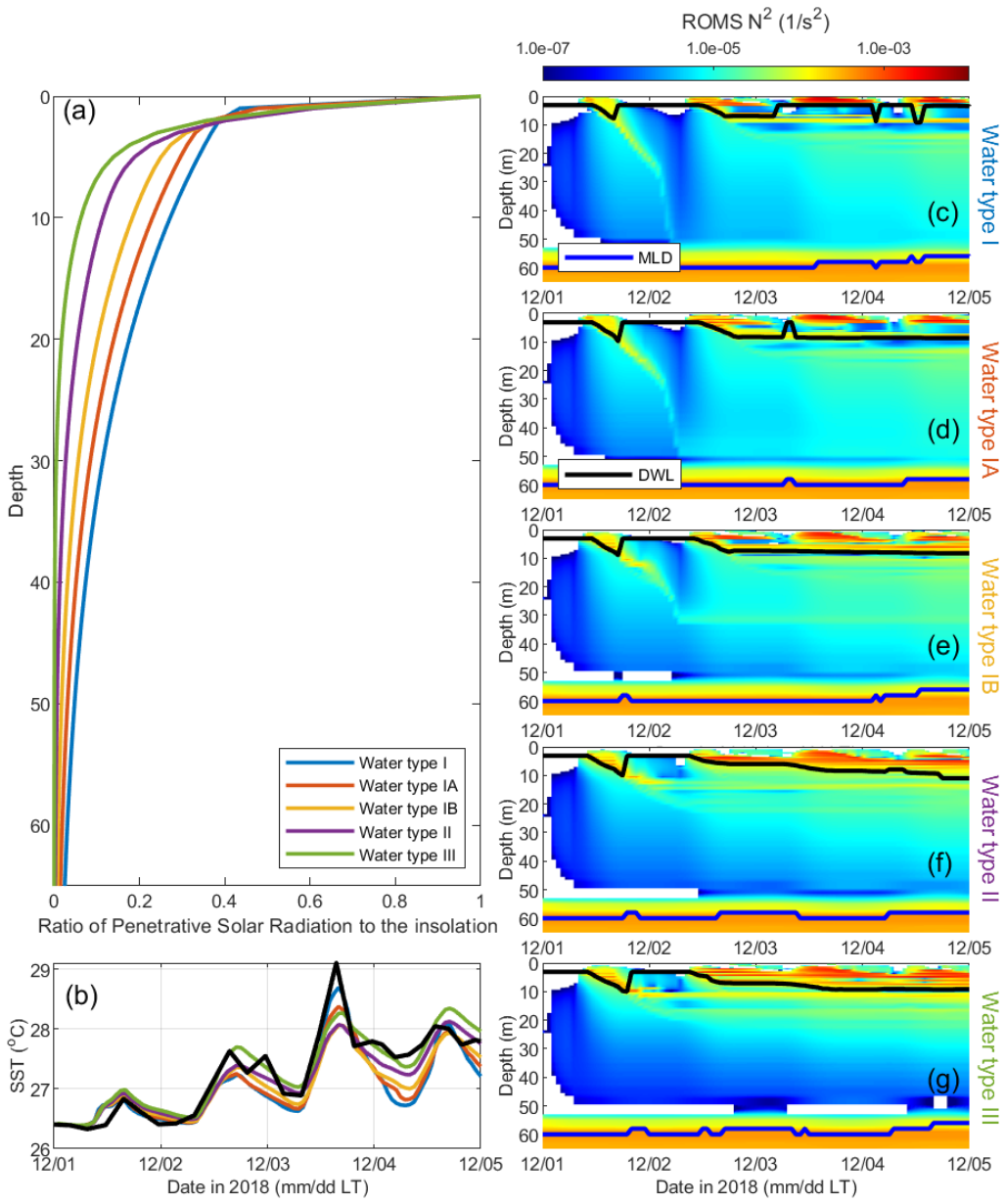

Fig. 9. Model results of N^2 (color shading in c-g) and SST (b) at float 9209 by varying the penetrative solar radiation based on five water types (colored lines in a and b). The DWL (black lines) and MLD (blue lines) are estimated in (c)-(g), respectively. The ratio of penetrative solar

814 radiation to the insolation at different depth during the model simulations is shown in (a). The
815 black line in (b) is the float-measured SST.

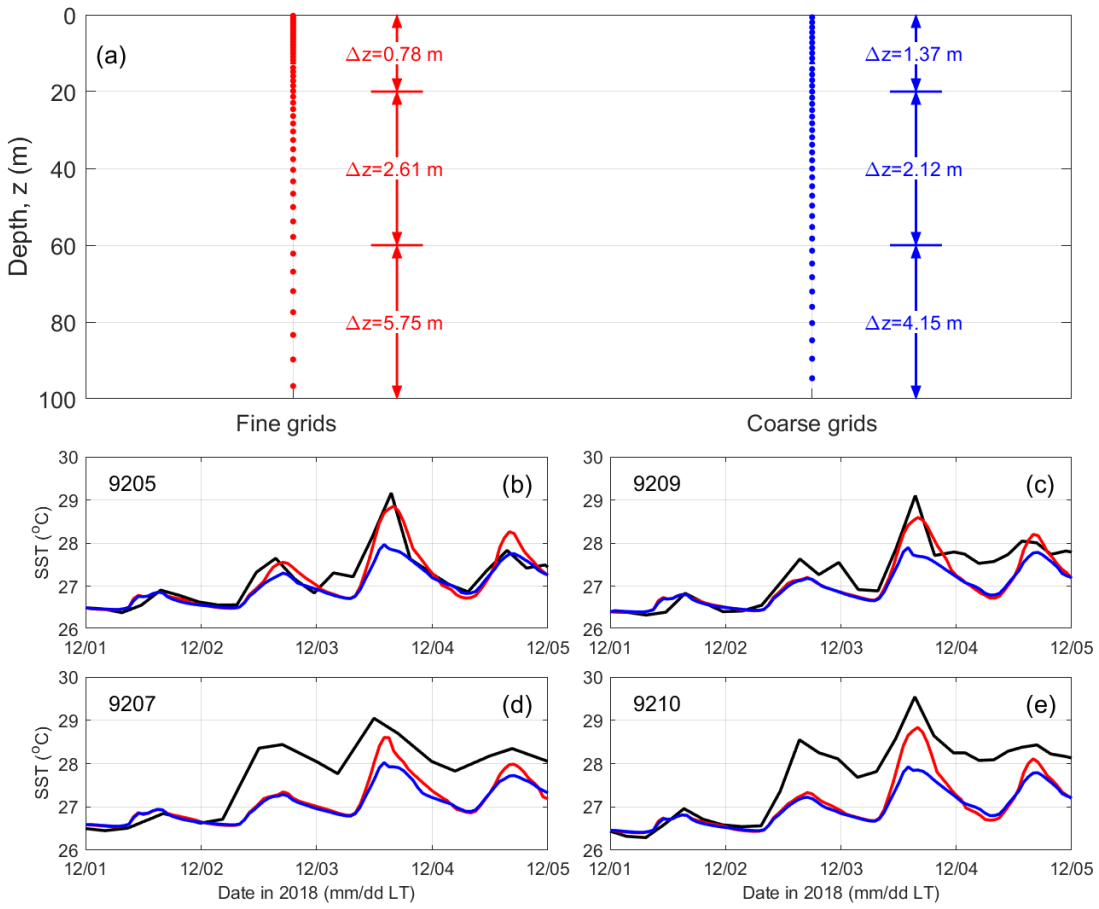

Fig. 10. Model results of SST at four ALAMO floats (b-e) simulated using two types of vertical grids (a) in the KPP: fine (red lines) and coarse grids (blue lines), with the comparsion to the float measurements (black lines), where Δz in (a) is the average of vertical resolution in different range of depth.

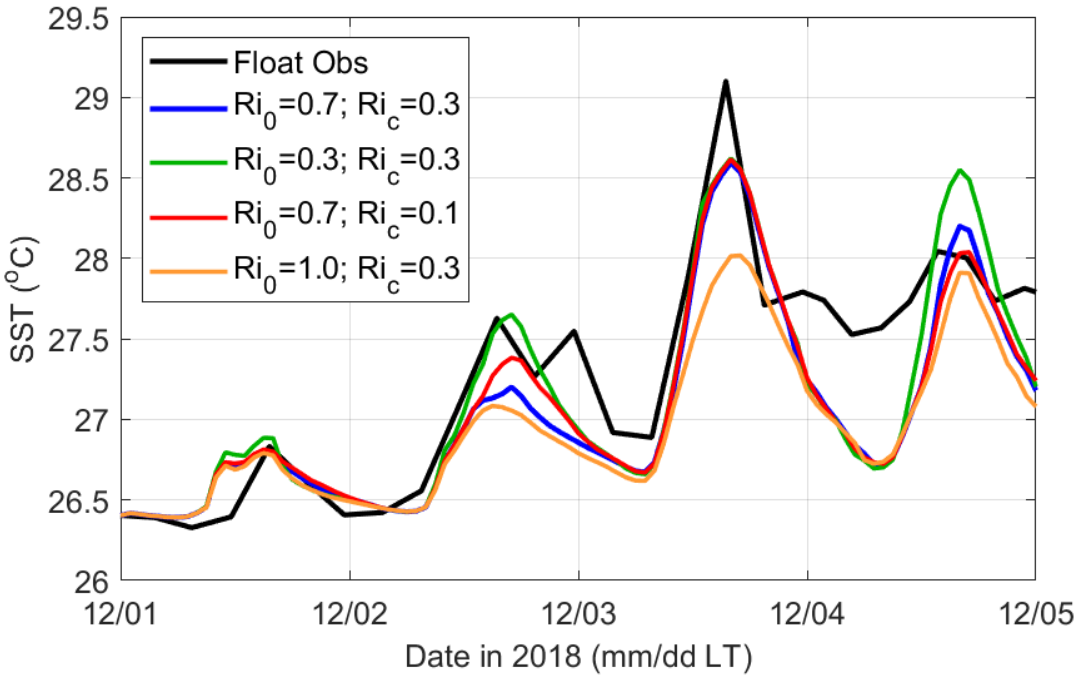

824

825

826 Fig. 11. Simulations of SST at float 9209 by different set of the mixing parameters Ri_0 and Ri_c

827 (blue: Ri_0 = 0.7 and Ri_c = 0.3; green: Ri_0 = 0.3 and Ri_c = 0.3; red: Ri_0 = 0.7 and Ri_c = 0.1; orange:

828 Ri_0 = 1.0 and Ri_c = 0.3), with the comparison to the float observation (black).

829

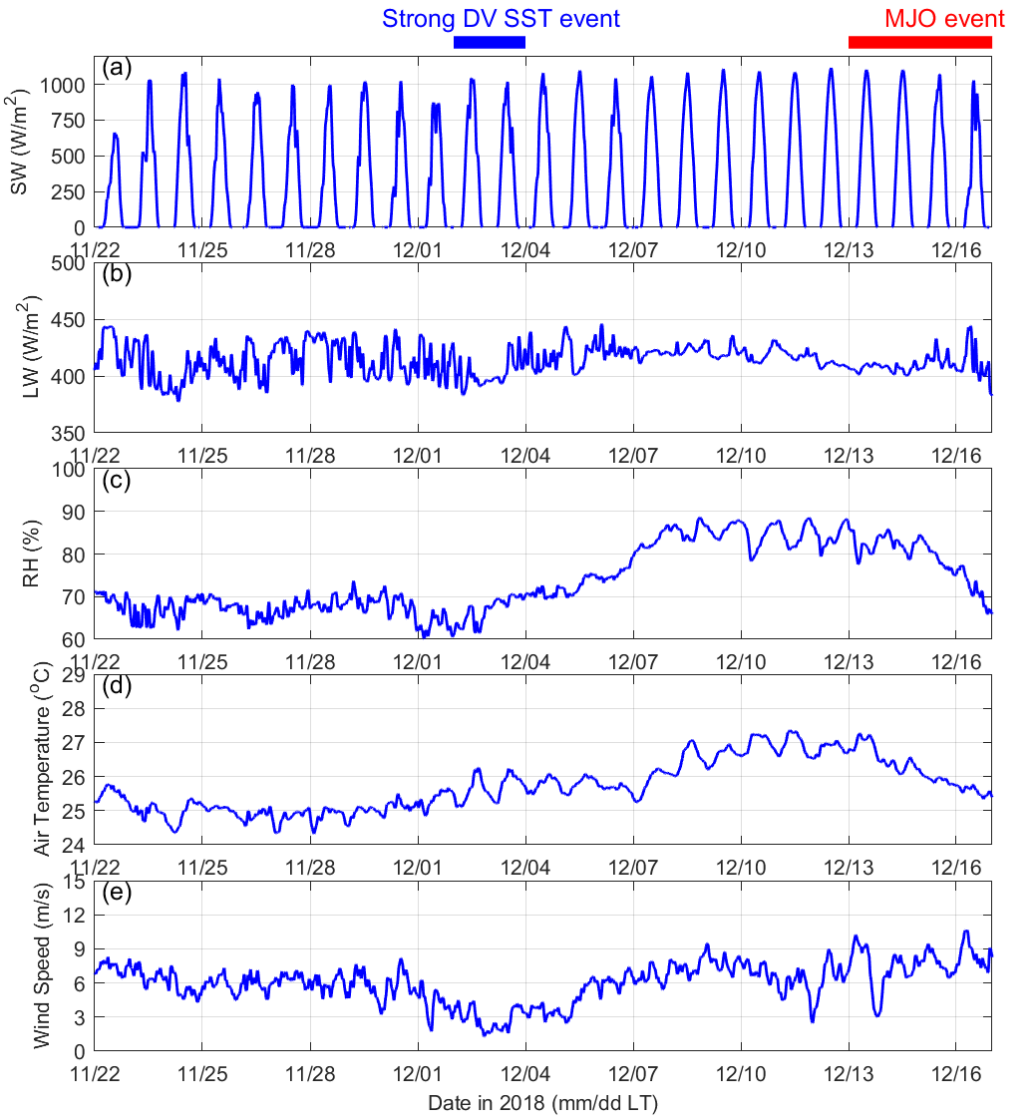

830

831 Fig. 12. Measurements of downward shortwave radiation SW (a), downward longwave radiation

832 LW (b), relative humidity RH at 3-m height above the sea surface (c), air temperature at 3-m

833 height above the sea surface (d), and wind speed at 4-m height above the sea surface (e) on the

834 FIO buoy. The period of the strong DV SST and MJO events are described in Feng et al. (2020).

835

836

837

Figure1.

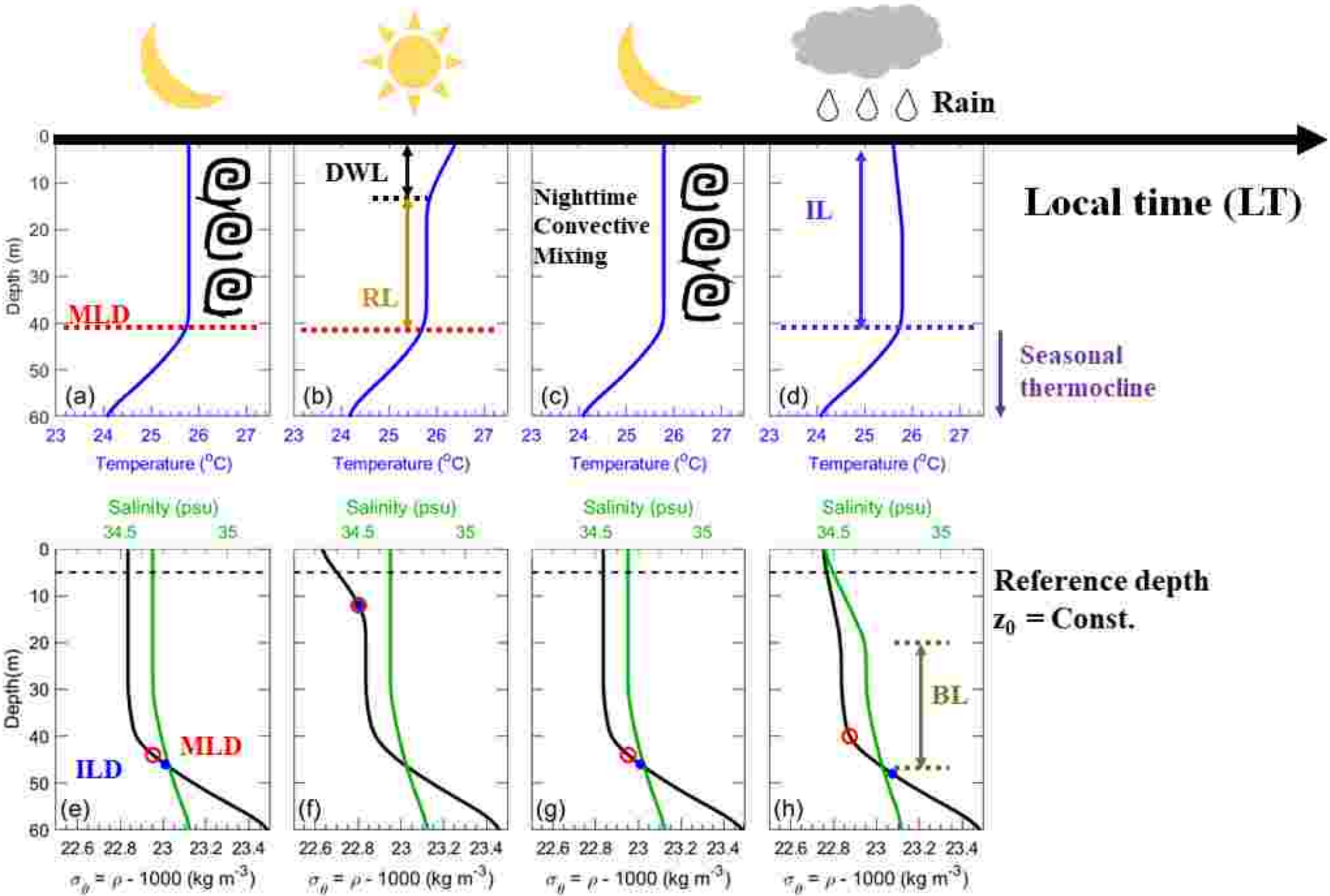
Rain
Local time (LT)
Depth (m)
DWL
RL
MLD
Nighttime
Convective
Mixing
IL
Seasonal
thermocline
(a)
(b)
(c)
(d)
Temperature (°C)
Salinity (psu)
ILD
MLD
BL
(e)
(f)
(g)
(h)
$\sigma_\theta = \rho - 1000$ (kg m^{-3})
Reference depth
z_0 = Const.

Figure2.

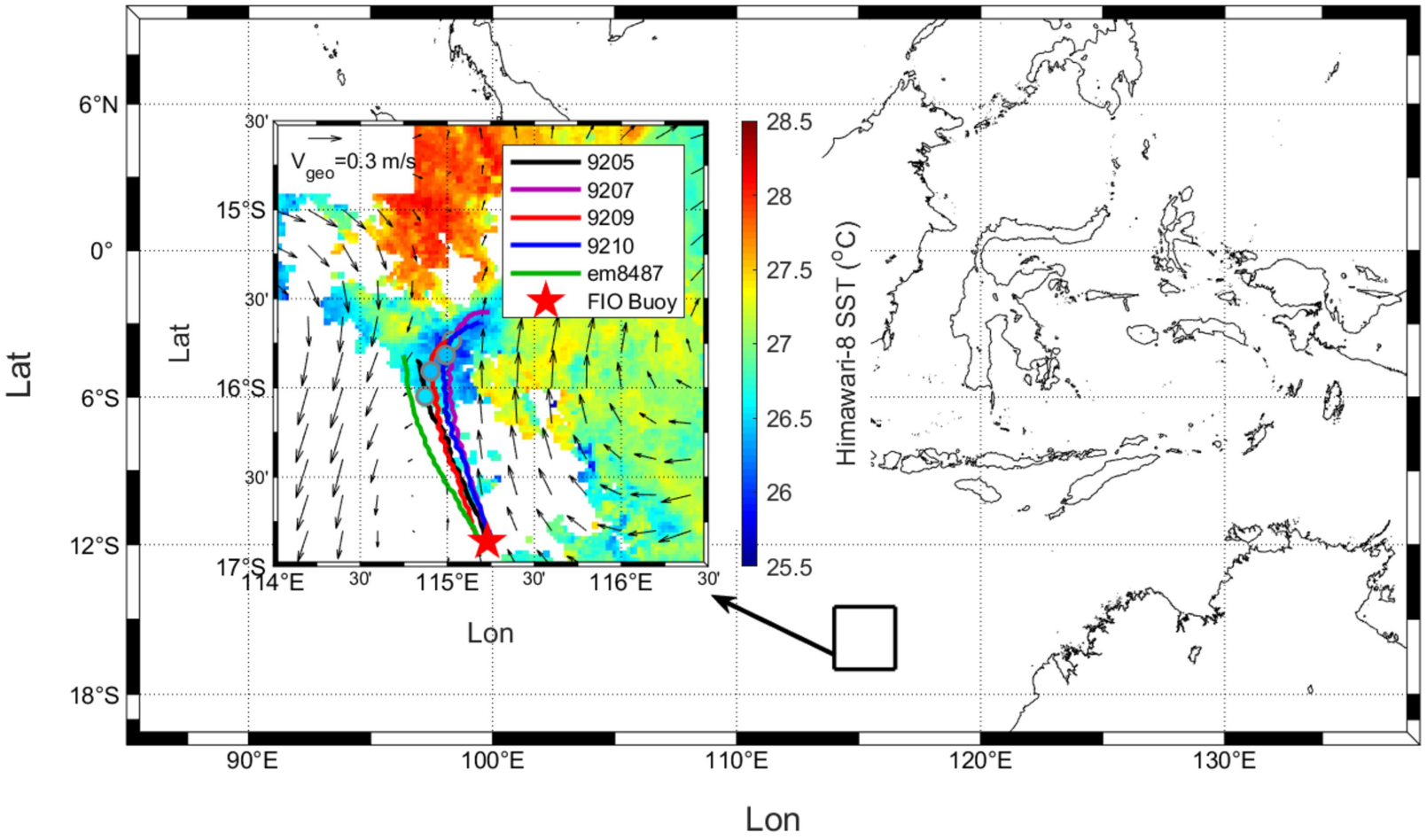
6°N
0°
6°S
12°S
18°S
Lat
90°E
100°E
110°E
120°E
130°E
Lon
30'
15°S
16°S
17°S
114°E
115°E
116°E
Lon
V_geo=0.3 m/s
9205
9207
9209
9210
em8487
FIO Buoy
28.5
28
27.5
27
26.5
26
25.5
Himawari-8 SST (°C)

Figure3.

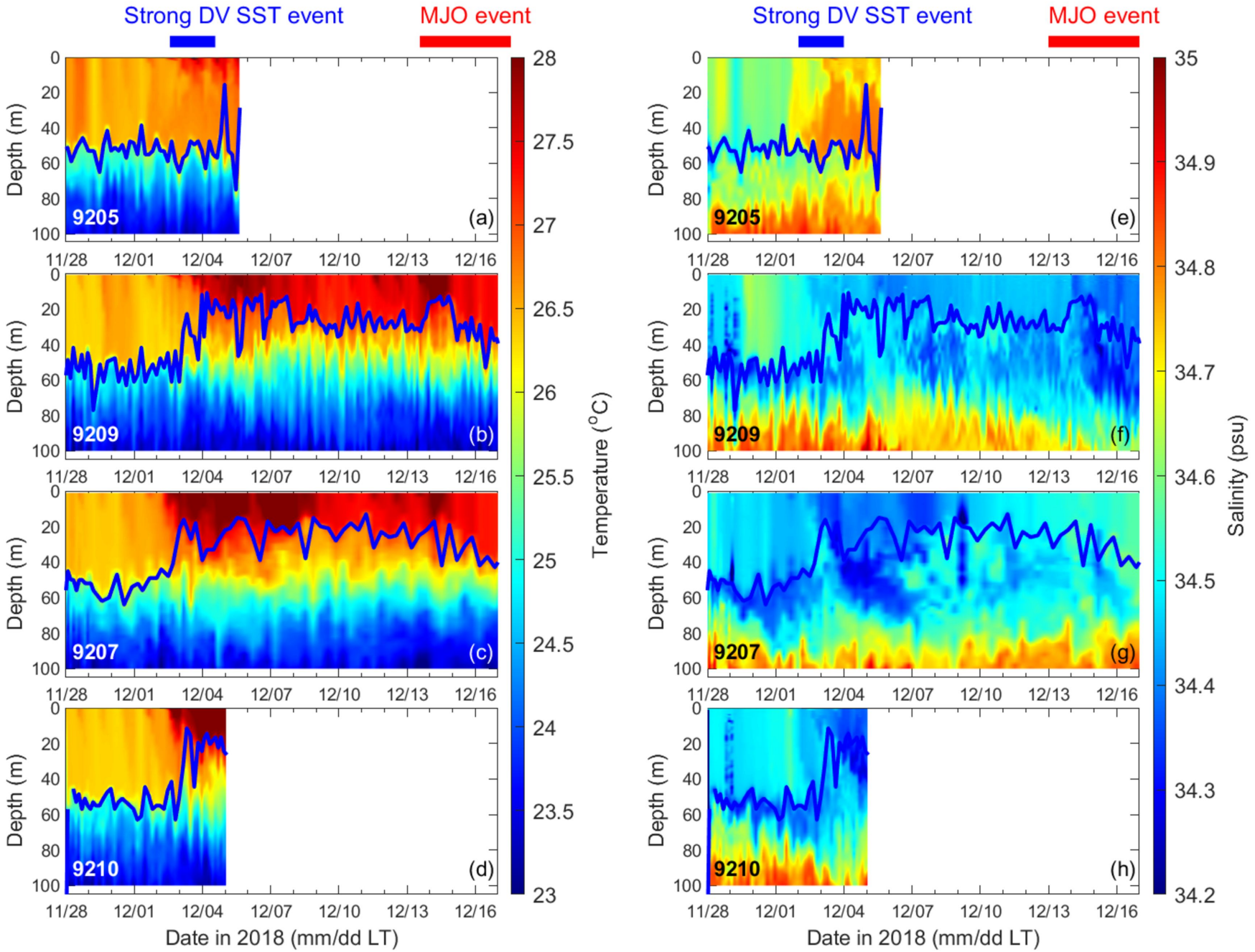
Strong DV SST event
MJO event
Depth (m)
9205
(a)
9209
(b)
9207
(c)
9210
(d)
11/28
12/01
12/04
12/07
12/10
12/13
12/16
Date in 2018 (mm/dd LT)
Temperature (°C)
28
27.5
27
26.5
26
25.5
25
24.5
24
23.5
23
(e)
(f)
(g)
(h)
Salinity (psu)
35
34.9
34.8
34.7
34.6
34.5
34.4
34.3
34.2

Figure4.

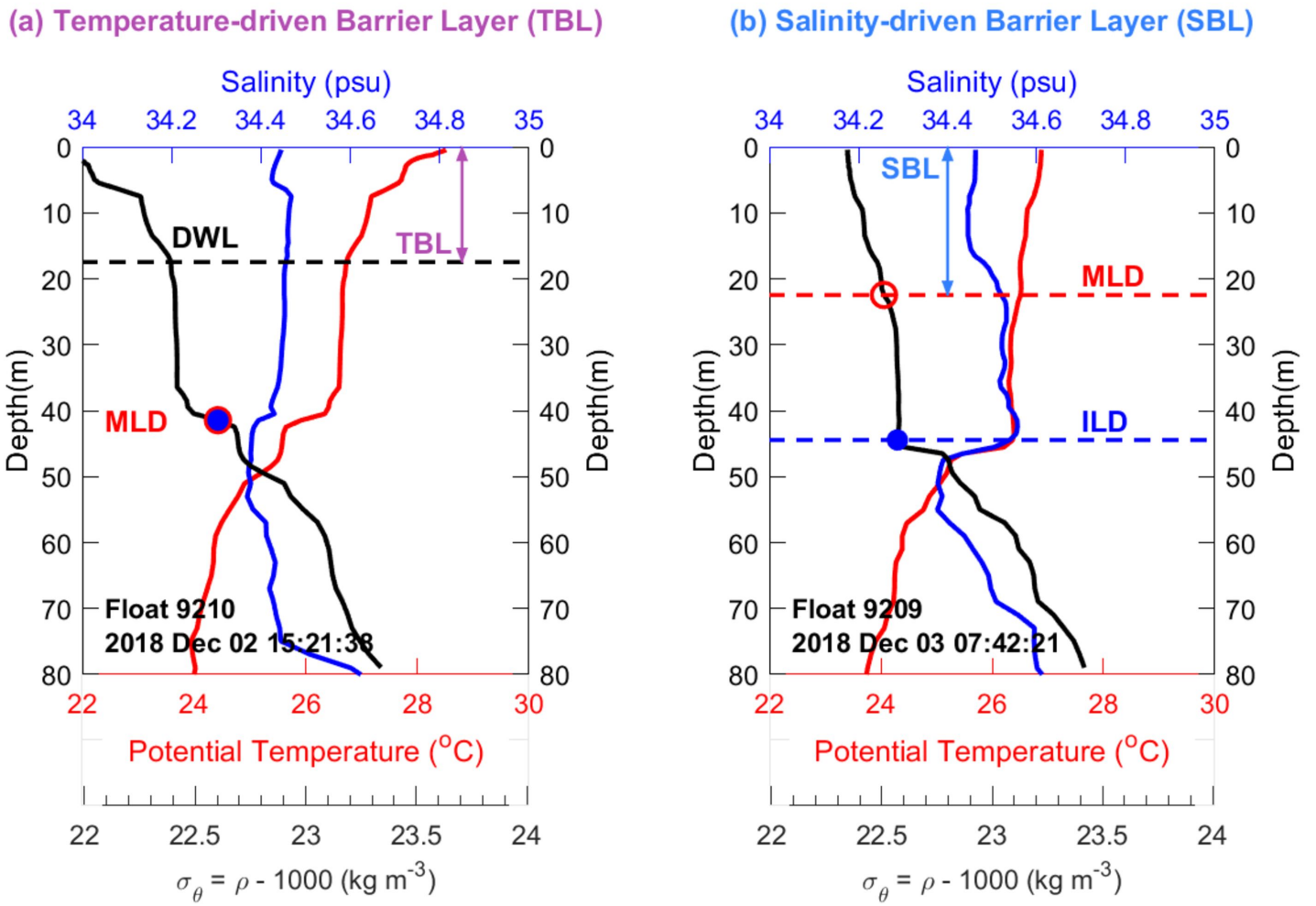
(a) Temperature-driven Barrier Layer (TBL)
Salinity (psu)
34
34.2
34.4
34.6
34.8
35
0
10
20
30
40
50
60
70
80
Depth(m)
DWL
TBL
MLD
Float 9210
2018 Dec 02 15:21:38
22
24
26
28
30
Potential Temperature (°C)
22
22.5
23
23.5
24
σ_θ = ρ - 1000 (kg m^{-3})
(b) Salinity-driven Barrier Layer (SBL)
Salinity (psu)
SBL
MLD
ILD
Float 9209
2018 Dec 03 07:42:21
Potential Temperature (°C)
σ_θ = ρ - 1000 (kg m^{-3})

Figure5.

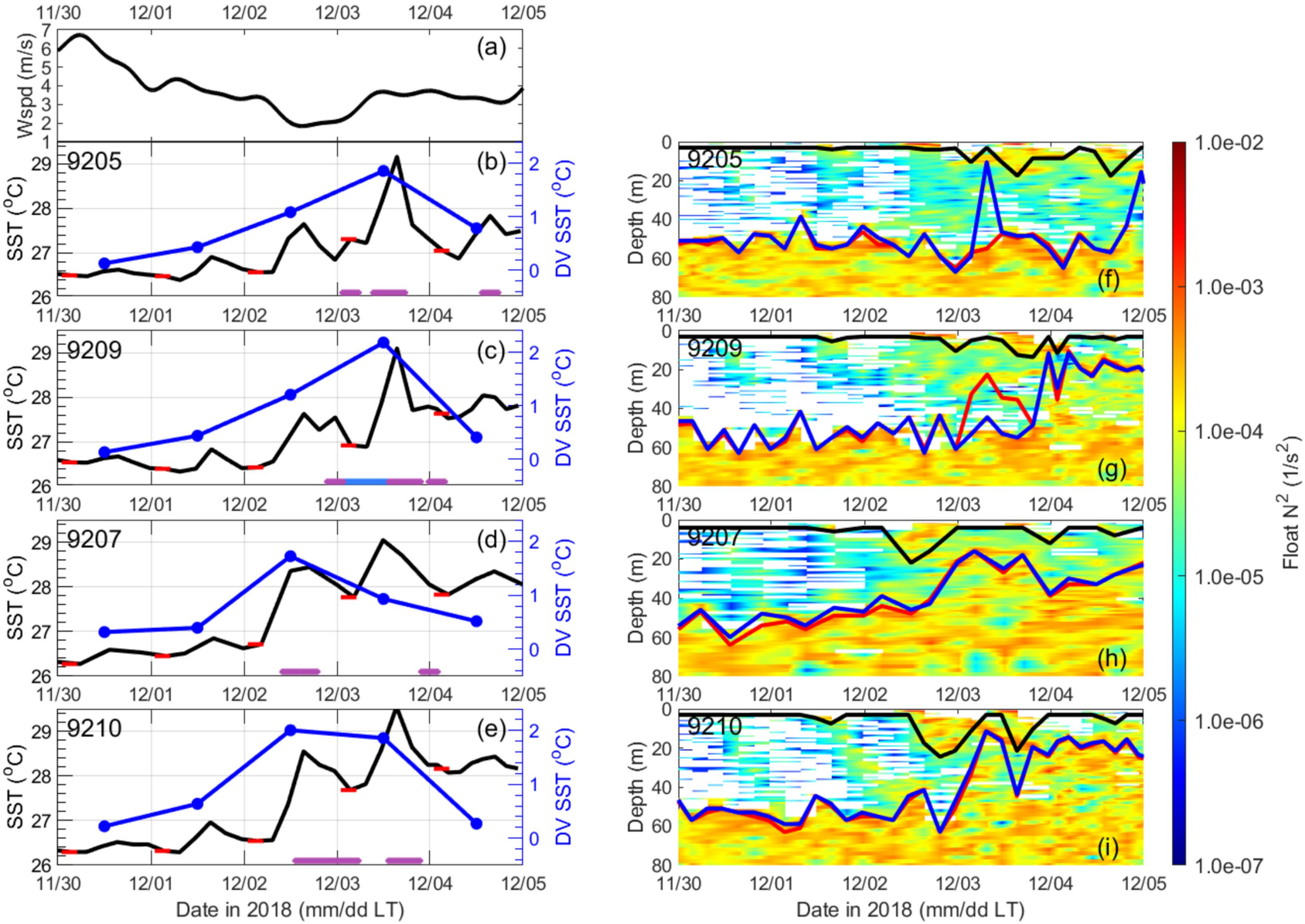
11/30
12/01
12/02
12/03
12/04
12/05
Wspd (m/s)
(a)
9205
(b)
9209
(c)
9207
(d)
9210
(e)
SST (°C)
DV SST (°C)
Date in 2018 (mm/dd LT)
Depth (m)
(f)
(g)
(h)
(i)
Float N² (1/s²)
1.0e-02
1.0e-03
1.0e-04
1.0e-05
1.0e-06
1.0e-07

Figure6.

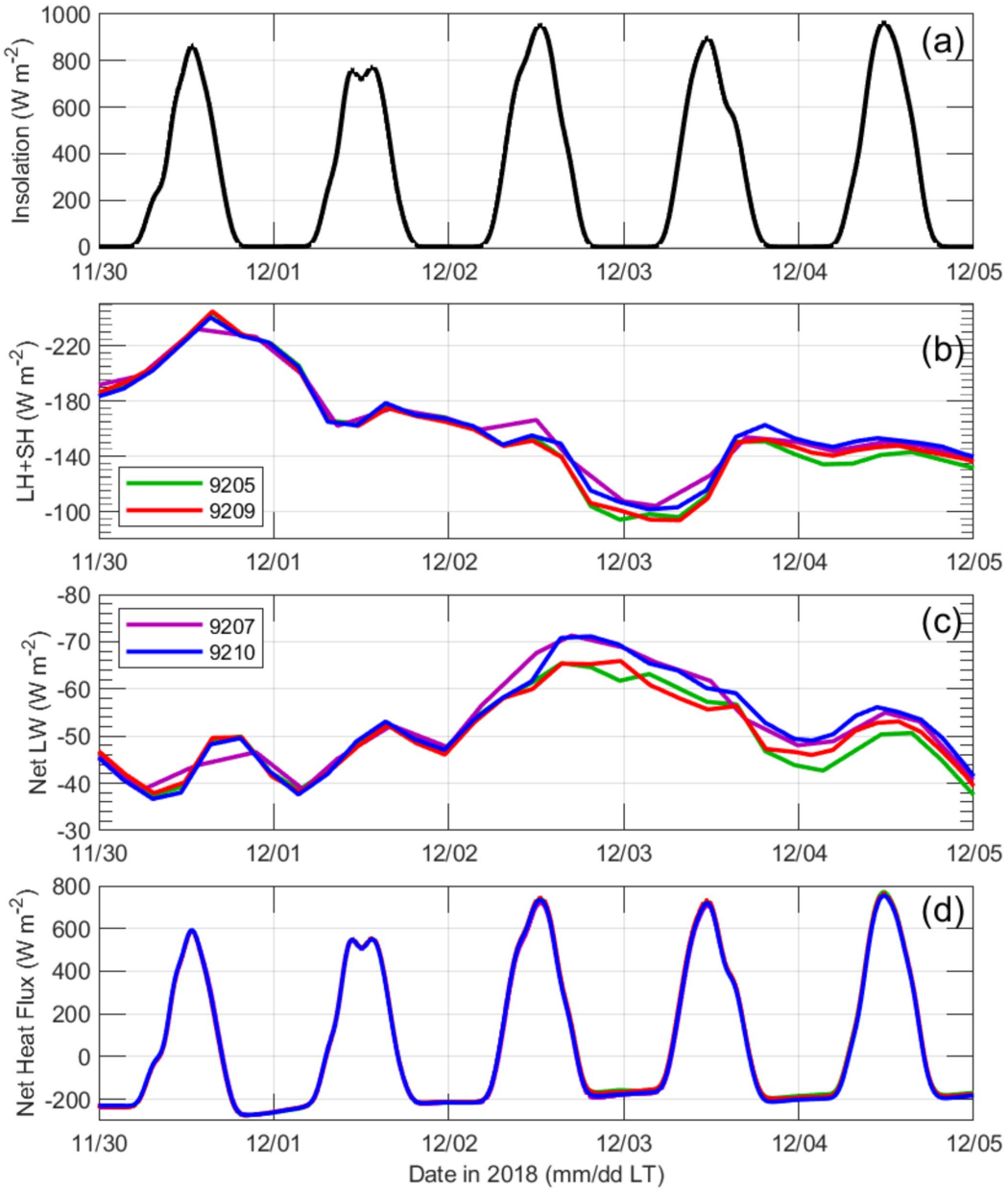
(a)
Insolation (W m-2)
1000
800
600
400
200
0
11/30
12/01
12/02
12/03
12/04
12/05
(b)
LH+SH (W m-2)
-220
-180
-140
-100
9205
9209
(c)
Net LW (W m-2)
-80
-70
-60
-50
-40
-30
9207
9210
(d)
Net Heat Flux (W m-2)
800
600
400
200
0
-200
Date in 2018 (mm/dd LT)

Figure7.

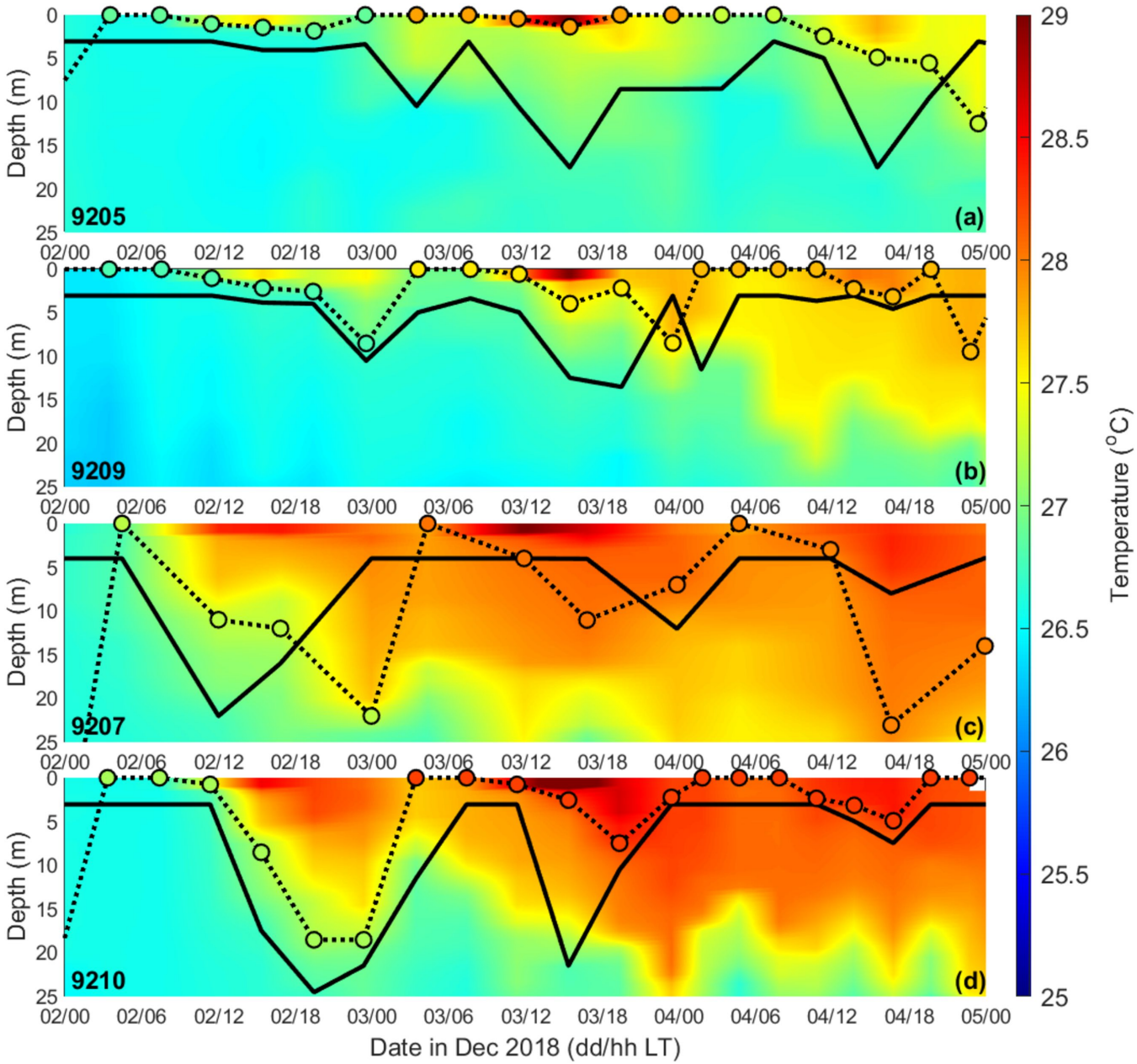
Depth (m)
0
5
10
15
20
25
9205
(a)
9209
(b)
9207
(c)
9210
(d)
02/00
02/06
02/12
02/18
03/00
03/06
03/12
03/18
04/00
04/06
04/12
04/18
05/00
Date in Dec 2018 (dd/hh LT)
Temperature (°C)
29
28.5
28
27.5
27
26.5
26
25.5
25

Figure8.

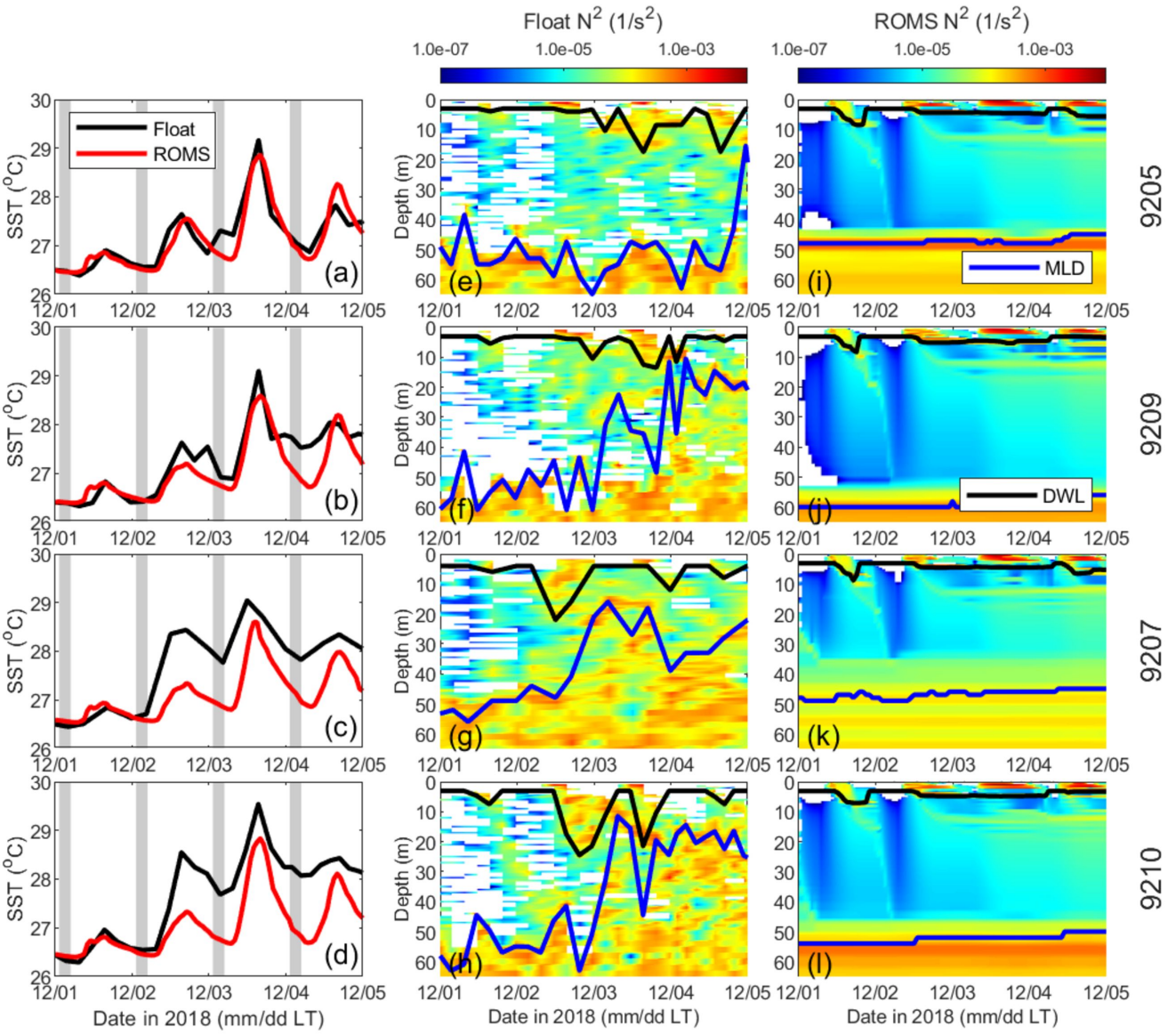
Float N^2 (1/s^2)
ROMS N^2 (1/s^2)
1.0e-07
1.0e-05
1.0e-03
Float
ROMS
MLD
DWL
SST (^{o}C)
Depth (m)
(a)
(b)
(c)
(d)
(e)
(f)
(g)
(h)
(i)
(j)
(k)
(l)
9205
9209
9207
9210
12/01
12/02
12/03
12/04
12/05
Date in 2018 (mm/dd LT)

Figure9.

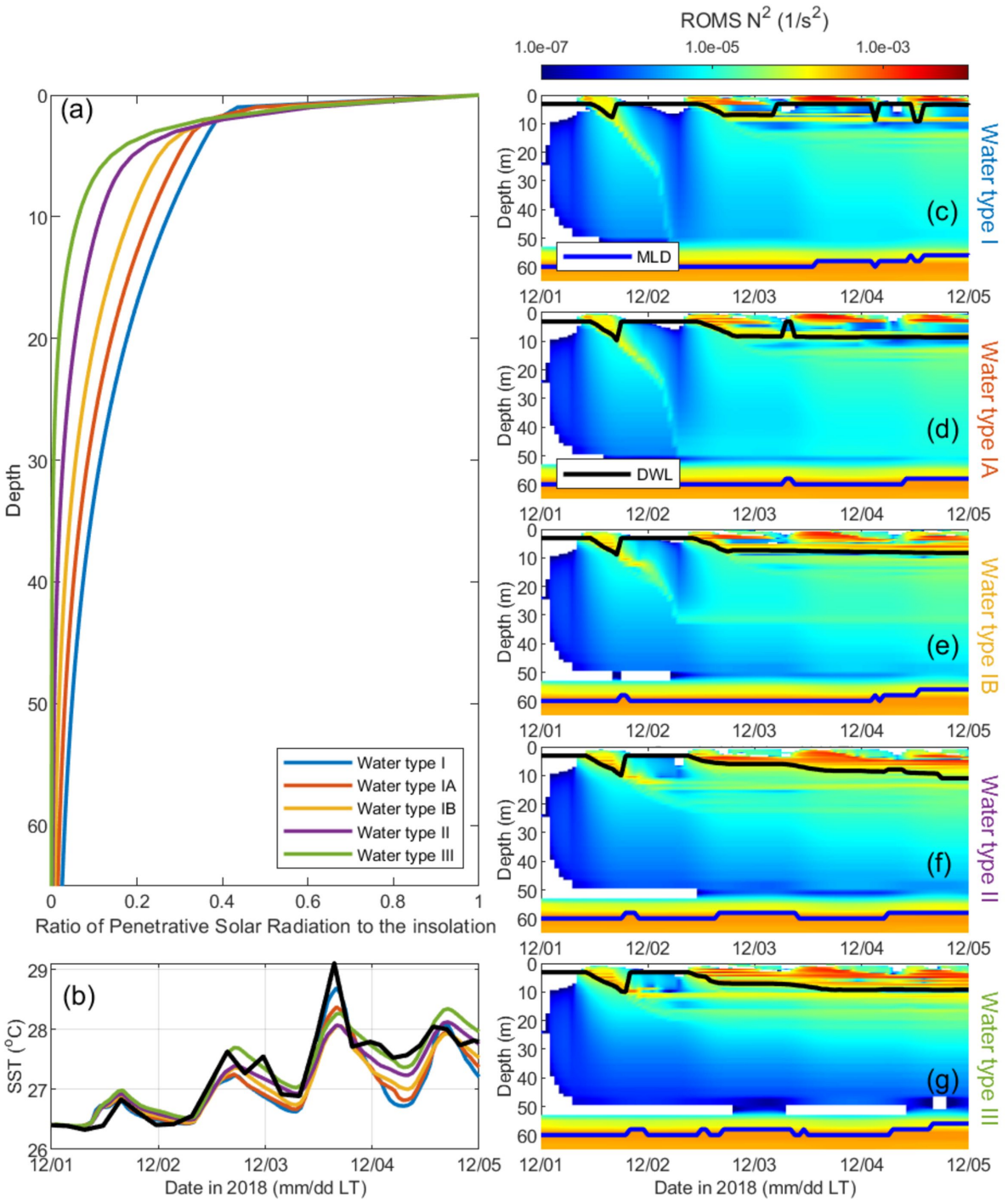
ROMS N^2 (1/s^2)
1.0e-07
1.0e-05
1.0e-03
(a)
Depth
Ratio of Penetrative Solar Radiation to the insolation
Water type I
Water type IA
Water type IB
Water type II
Water type III
(b)
SST (°C)
Date in 2018 (mm/dd LT)
(c)
(d)
(e)
(f)
(g)
MLD
DWL
Depth (m)
12/01
12/02
12/03
12/04
12/05
Water type I
Water type IA
Water type IB
Water type II
Water type III

Figure10.

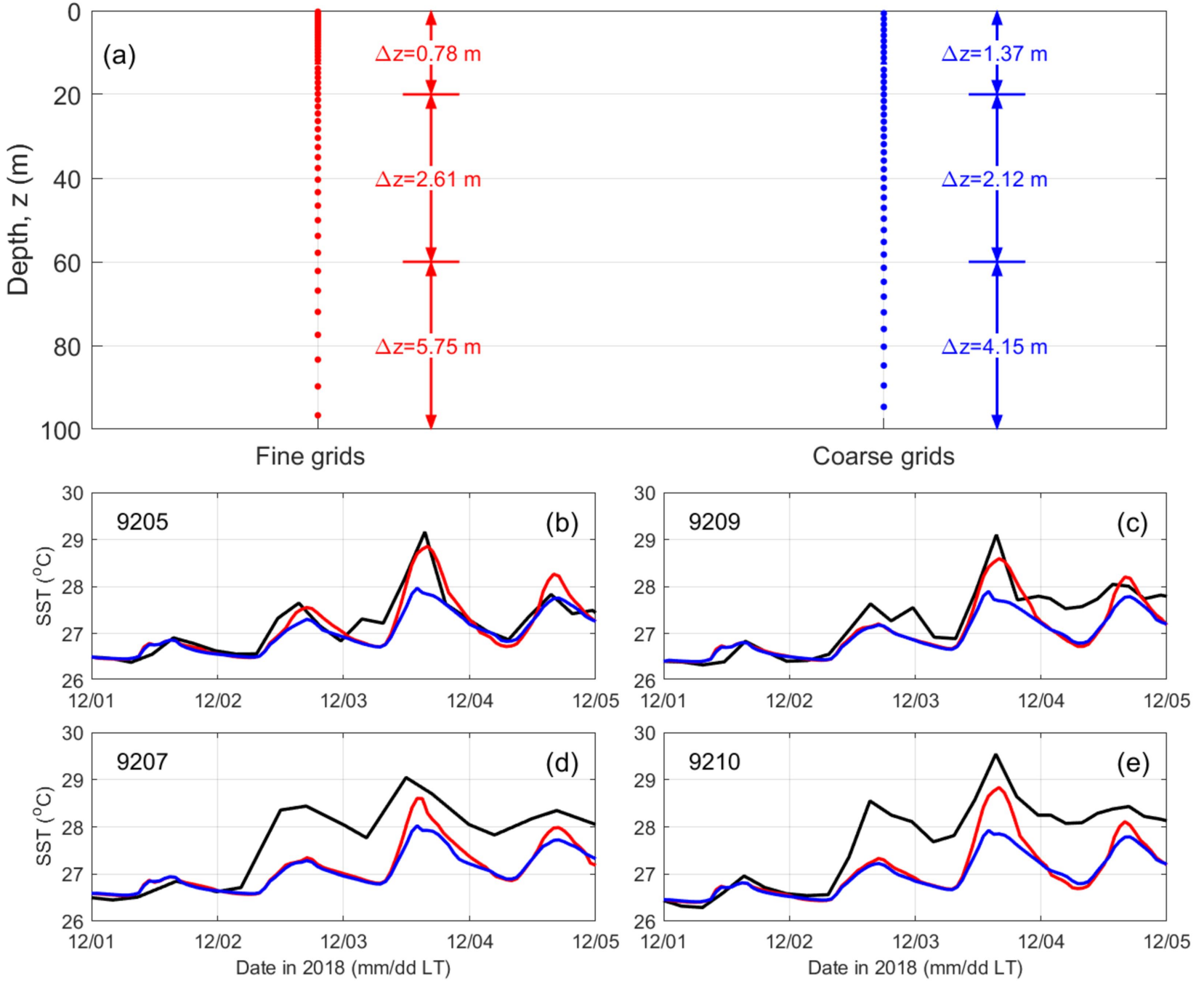
(a)
Δz=0.78 m
Δz=2.61 m
Δz=5.75 m
Δz=1.37 m
Δz=2.12 m
Δz=4.15 m
Depth, z (m)
0
20
40
60
80
100
Fine grids
Coarse grids
9205
(b)
9209
(c)
9207
(d)
9210
(e)
SST (°C)
26
27
28
29
30
12/01
12/02
12/03
12/04
12/05
Date in 2018 (mm/dd LT)

Figure11.

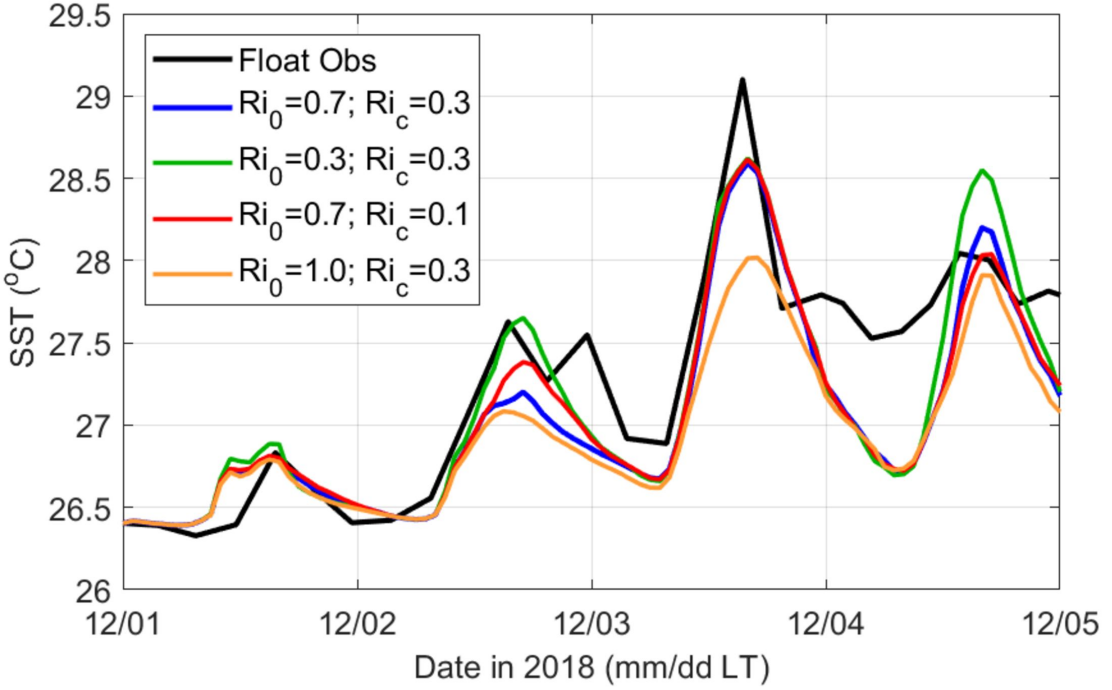
Float Obs
Ri0=0.7; Ric=0.3
Ri0=0.3; Ric=0.3
Ri0=0.7; Ric=0.1
Ri0=1.0; Ric=0.3
SST (°C)
29.5
29
28.5
28
27.5
27
26.5
26
12/01
12/02
12/03
12/04
12/05
Date in 2018 (mm/dd LT)

Figure12.

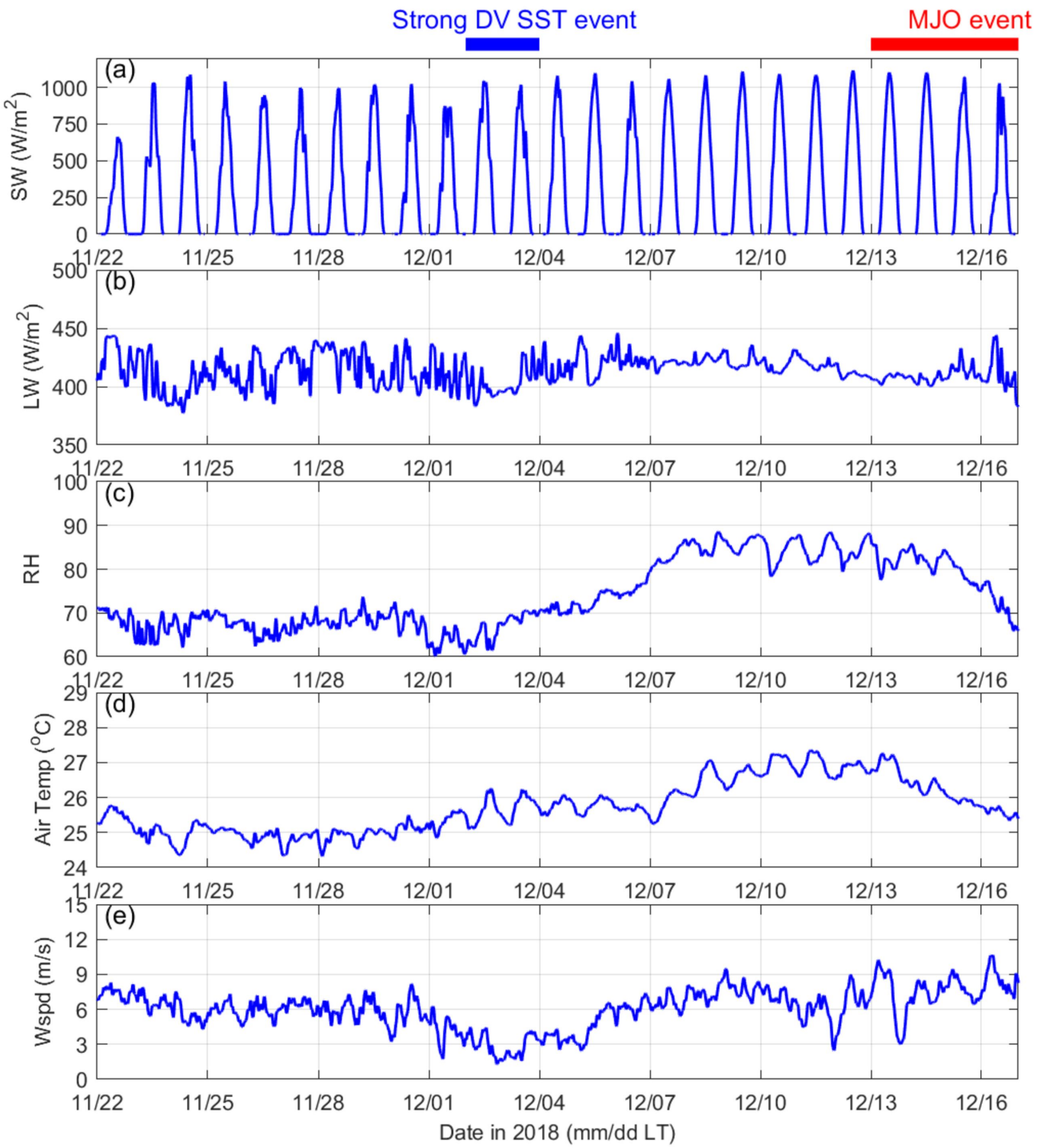
Strong DV SST event
MJO event
(a)
SW (W/m2)
1000
750
500
250
0
11/22
11/25
11/28
12/01
12/04
12/07
12/10
12/13
12/16
(b)
LW (W/m2)
500
450
400
350
(c)
RH
100
90
80
70
60
(d)
Air Temp (oC)
29
28
27
26
25
24
(e)
Wspd (m/s)
15
12
9
6
3
0
Date in 2018 (mm/dd LT)